Prior to publication in a peer-reviewed journal, please cite this manuscript as:
Manning, C.C.M., A. Payyambally, J.L. Mottram, and K. Ward, Methane and nitrous oxide concentrations and sea-air fluxes in western Long Island Sound, a eutrophic urban estuary: Hourly to seasonal variability, *EarthArXiv*, https://doi.org/10.31223/X54T8Z

Methane and nitrous oxide concentrations and sea-air fluxes in western Long Island Sound, a eutrophic urban estuary: Hourly to seasonal variability

Cara C. M. Manning[1], Anagha Payyambally[1], Josie L. Mottram[1], and Kelsey Ward[1]
[1]University of Connecticut, Department of Marine Sciences, Groton, CT, 06340, USA
Correspondence to: Cara C. M. Manning (cara.manning@uconn.edu)

Abstract. We report the first water column profiles of dissolved methane (CH_4) and nitrous oxide (N_2O) in western Long Island Sound, an urban estuary in which seasonal hypoxia occurs due to eutrophication and restricted exchange with the ocean. We collected samples at seven stations along an 18 km transect in August 2023, October 2023, and May 2024. CH_4 concentrations and sea-air fluxes were highest in August (mean concentration 101 nmol kg^{-1} and mean sea-air flux 154 μmol m^{-2} d^{-1}) and lowest in May (mean concentration 32 nmol kg^{-1} and mean sea-air flux 62 μmol m^{-2} d^{-1}). Conversely, N_2O concentrations and sea-air fluxes were highest in May (mean concentration 12.0 nmol kg^{-1} and mean sea-air flux 4.8 μmol m^{-2} d^{-1}) and lowest in August (mean concentration 10.1 nmol kg^{-1} and mean sea-air flux 2.5 μmol m^{-2} d^{-1}). Surface concentrations and sea-air fluxes of CH_4 and N_2O were highest at the westernmost station (closest to New York City) in all three seasons. To investigate short-term variability in CH_4, N_2O, and oxygen (O_2), we collected samples every 4 hours over 28 hours at the middle station of the transect, in all three months. By evaluating the relationship between the dissolved gas concentrations, tidal stage and sampling time relative to solar noon, we concluded that there is measurable short-term variability in all three gases, and that the drivers of variability in these dissolved gases are complex and not dominated by tides or light levels alone. Our data suggest that there is a persistent source of surface water to western Long Island Sound with high concentrations of CH_4 and N_2O which drives an along-sound gradient in surface concentrations and sea-air fluxes.

Keywords: methane; nitrous oxide; oxygen; hypoxia; estuary; diel cycle

1. Introduction

Long Island Sound (LIS) is an urban estuary that receives wastewater discharge from the most populous city in the USA, New York City, and undergoes seasonal hypoxia. Hypoxic conditions, often defined as dissolved oxygen (O_2) concentrations lower than ~64 μmol L^{-1} (~2 mg L^{-1}), can be harmful or fatal to a range of marine life (Diaz and Rosenberg, 2008; Vaquer-Sunyer and Duarte, 2008). Eutrophication (excess nitrogen inputs from human activities, including point source wastewater discharge and runoff) contributes to hypoxia in LIS by driving the overproduction of photosynthetic organisms at the surface and subsequent the removal of O_2 at depth from decomposition (Parker and O'Reilly, 1991; Varekamp et al., 2014).

Regionally, hypoxia is most severe in western LIS due to the restricted circulation and proximity to the high population density and associated wastewater inputs from New York City (Lee and Lwiza, 2008; Whitney and Vlahos, 2021). The East River is a tidal estuary between the island of Manhattan and Brooklyn/Queens which discharges Hudson River water and New York City wastewater into western LIS (Figure 1). There are currently six wastewater treatment plants in the East River which collectively discharge wastewater from 4 million of the 8 million residents of New York City (NYCDEP, 2025). These wastewater treatment plants contributed a nitrogen (N) loading of 2×10^6 kg N y^{-1} in 2016, accounting for >95% of the total N load from the East River, and ~18% of the total N loading to LIS in 2016 (Vaudrey, 2017) and ~11% of the N load to LIS from 1995−2016 (Vlahos et al., 2020). LIS is an atypical estuary with respect to the location of the freshwater discharge; the largest source of freshwater is the Connecticut River (mean discharge ~500 m^3 s^{-1}), which is located on the northeastern end of the estuary, close to the mouth (Gay et al., 2004). For western LIS, located at the head of the estuary, the East River is the largest source of freshwater despite its volume flux being smaller, with a mean surface advective flux of ~260 m^3 s^{-1} (Gay et al., 2004; Vlahos et al., 2020). The majority of the N load from larger rivers in the eastern and central LIS does not enter western LIS (Vlahos et al., 2020). For western LIS, Vlahos et al. (2020) determined that the East River is likely the largest source of nitrogen, contributing $(3.2 \pm 2.2) \times 10^6$ kg N y^{-1}, as compared to other rivers which contributed $(2.6 \pm 0.8) \times 10^6$ kg N y^{-1}, atmospheric deposition which contributed $(1.2 \pm 0.2) \times 10^6$ kg N y^{-1}, and lateral transport from central LIS which contributed $(0.3 \pm 1.7) \times 10^6$ kg N y^{-1} for the period 1995−2016; note that N inputs decreased over this period. The study of Vlahos et al. (2020) defined western LIS to include all areas west of the Housatonic River; since our study focuses on only the westernmost half of this region, the influence of the East River will be even more prominent (Figure 1). Prior observations in the East River have demonstrated elevated nutrient levels associated with wastewater input in this system (Bowman, 1977; Li et al., 2018; Wallace, 2020). Wastewater treatment plant upgrades over recent decades have reduced the amount of nitrogen (N) pollution entering LIS by ~60% from the year 2000 baseline and reduced the 5-year averaged overall hypoxic area in LIS. However, hypoxia continues to occur annually in western LIS and the hypoxic area in the far western sound actually increased from 2017 to 2023 (Duvall et al., 2024; Whitney and Vlahos, 2021). Ongoing and future climate change contributes to the persistence of hypoxia in western LIS: warming temperatures reduce the solubility of O_2 in water and may also increase respiration rates and stratification (Irby et al., 2018; Parker and O'Reilly, 1991; Whitney and Vlahos, 2021; Wilson et al., 2008). Other temperate urban estuaries experience similar interacting stressors from nutrient pollution and climate change (Howarth et al., 2011; Irby et al., 2018).

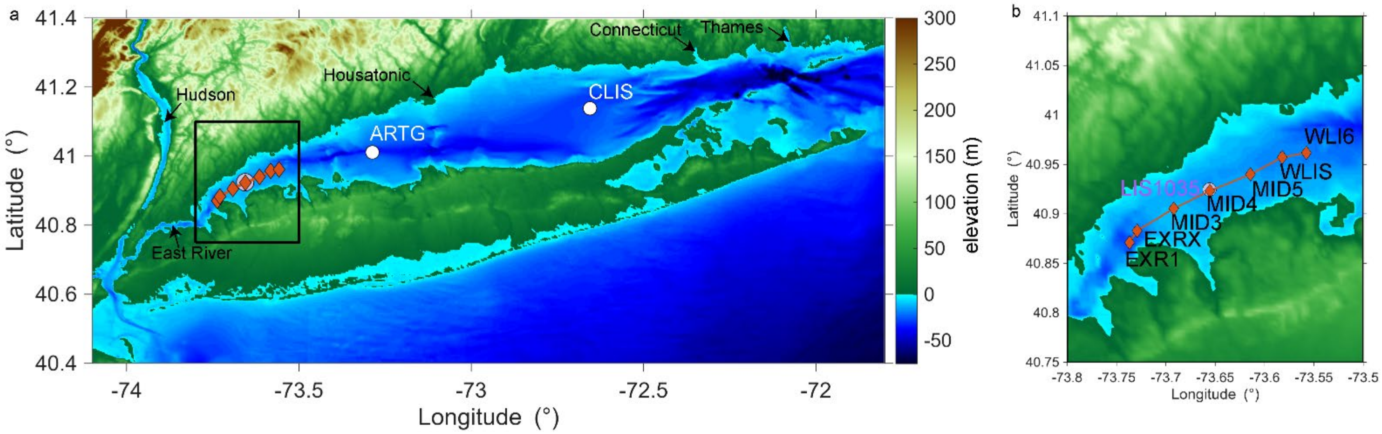

Figure 1. Maps of Long Island Sound (a) and the transect sampled (b).

The locations of stations sampled on each cruise are shown as orange diamonds and the stations sampled only in May 2024 (ARTG and CLIS) are shown with black circles (a). The station used for current speed predictions (LIS1035), near MID4, is shown with a purple circle. Large rivers influencing LIS are shown with black arrows (the Hudson, Housatonic, Connecticut, Thames, and East River). Elevation data was retrieved from The GEBCO Grid (GEBCO Compilation Group, 2024).

Alt Text: Map of the study area showing elevation above and below sea level and the locations of the stations at which data was collected. One panel shows all of LIS and the other shows the region near 40.9° N, 73.65° W where the water sampling transect was centered.

Biochemical reactions involved in organic matter production and decomposition are associated with the production and/or consumption of greenhouse gases including carbon dioxide (CO_2), methane (CH_4), and nitrous oxide (N_2O) (Bange et al., 2010; Reeburgh, 2007). Although the atmospheric concentrations of CH_4 and N_2O are lower than CO_2, CH_4 and N_2O trap heat more effectively and have higher global warming potentials (Forster et al., 2021). Reported emissions of CH_4 and N_2O are widely variable across different coastal and estuarine systems (Capelle and Tortell, 2016; Harley et al., 2015; Kock et al., 2016; Naqvi et al., 2010; Robinson et al., 1998; Rosentreter et al., 2021; Seitzinger et al., 2000; de Wilde and de Bie, 2000; Zheng et al., 2022). For example, a recent global meta-analysis reported that published estuarine sea-air gas fluxes range from approximately 0 to 50000 $\mu mol\ m^{-2}\ d^{-1}$ for CH_4 and −60 to 500 $\mu mol\ m^{-2}\ d^{-1}$ for N_2O (Zheng et al., 2022). Although measurements of benthic N_2O production and groundwater-associated fluxes in LIS have been reported (Mazur et al., 2021; Young et al., 2016), to our knowledge there are no published water column measurements of N_2O or CH_4 concentrations or sea-air fluxes of these gases in LIS.

CH_4 is produced and consumed through anaerobic and aerobic processes (Reeburgh, 2007). It is produced during anaerobic methanogenesis, an organic matter respiration process that uses carbon as an electron acceptor and result in the formation of CH_4. Anaerobic methanogenesis has previously been reported in LIS sediments in some of the earliest work on marine sedimentary organic matter diagenesis (Martens and Berner, 1974, 1977). Recent work has demonstrated that CH_4 supersaturation in the near-surface ocean may be linked to processes associated with photosynthesis and metabolism of methylated phosphorus and/or sulfur species (Damm et al., 2015; Fazi et al., 2021; Perez-Coronel and Beman, 2022; Repeta et al., 2016). Another study reported that some methylotrophic methanogens inhabiting coastal sediments are oxygen tolerant, and thus CH_4 production may continue even under oxic conditions (Hall et al., 2025). Currently, the relative importance of aerobic versus anaerobic CH_4 production to the CH_4 balance in eutrophic estuarine systems is not well known. In anaerobic systems, CH_4 is converted to CO_2 through anaerobic oxidation, in which other electron donors such as sulfate (SO_4^{2-}) or nitrate (NO_3^-) are oxidized. This process occurs in anaerobic sediments, and potentially particles, and regulates the amount of CH_4 available to diffuse into the overlying water column. In oxygenated systems, CH_4 is consumed through aerobic oxidation (methanotrophy), conducted by organisms who use CH_4 as their carbon source for organic matter synthesis (Mau et al., 2013; Ward et al., 1987). Methanotrophy can significantly reduce sea-air fluxes of CH_4 (Mau et al., 2013).

N_2O is generated as a byproduct during ammonium oxidation, the first step of nitrification, a chemoautotrophic process that yields energy from the conversion of ammonium to nitrite (NH_4^+ to NO_2^-) (Ward, 2008). Additionally, N_2O is an intermediate in heterotrophic denitrification, an anaerobic organic matter degradation process (Bange et al., 2010). Depending on environmental conditions, this reaction can either be a net source or sink of N_2O, with suboxic conditions tending to favor net N_2O production (incomplete denitrification) and anoxic conditions favoring N_2O consumption (complete denitrification) (Bange et al., 2010; Kock et al., 2016). Additionally, nitrification and denitrification can be coupled through the process of nitrifier denitrification, where the oxidation of NH_4^+ to NO_2^- is followed by reduction of NO_2^- to nitrogen gas (N_2) through intermediates, including N_2O (Wrage et al., 2001).

The objectives of this study were to obtain the first measurements of CH_4 and N_2O concentrations in LIS, to calculate their sea-air fluxes, and to characterize seasonal to hourly variability in CH_4 and N_2O in LIS. In coastal systems, biogeochemical parameters can vary on sub-daily timescales due to both physical and biological forcing (e.g., due to daily changes in tidal phase and light levels), but this variability has rarely been explored for CH_4 and N_2O. We evaluated how sampling time influences the concentrations and calculated fluxes. We determined the contribution of CH_4 and N_2O to the C and N budgets for LIS and converted the CH_4 and N_2O fluxes to CO_2-equivalents to compare the fluxes with previously-published CO_2 data for western LIS. We place the results of this study in the context of other estuarine studies and discuss potential drivers of the observed trends. Western LIS is a seasonally hypoxic urban estuary undergoing ongoing change due to anthropogenic forcing, as is common among estuaries worldwide, and the results in this study have relevance to understanding greenhouse gas dynamics in such systems today and in the future.

2. Methods

2.1 Sampling locations, timing, and procedures

We collected samples during cruises on the R/V *Connecticut* (2–3 August 2023, 19–20 October 2023, and 22–23 May 2024). On each cruise, we collected water column profiles at the same seven stations spanning an ~18 km transect. The transect stations were sampled on day 2 over a ∼6-hour period, beginning at approximately 07:00 local time at the westernmost station (EXR1) and proceeding sequentially toward the easternmost station (WLI6). Two of the stations were sampled repeatedly: station MID4 was sampled every four hours over a 28-h period (eight times in total, beginning at ~08:00 on day 1 and continuing until ~12:00 on day 2), and station EXRX was sampled at ~09:00 on day 1 and day 2. For both EXRX and MID4, the final profile was collected as part of the seven-station transect on day 2. Station depths ranged from 13 to 32 m.

Additionally, during the May 2024 cruise only, we sampled at stations CLIS and ARTG following the sample collection at WLI6 on day 2. Stations CLIS and ARTG had unique hydrographic properties due to their location closer to the mouth of the estuary. To identify seasonal variability using a consistent dataset, the observations at stations CLIS and ARTG are not included in the discussion and visualizations of this manuscript but are included in the datasets archived to PANGAEA (Manning et al., 2026).

Water samples were collected from Niskin bottles attached to a rosette with a CTD (Sea-Bird Electronics SBE 9 with SBE 43 O_2 sensor). Additionally, to get near-bottom water at each station, a Niskin bottle was lowered by hand to ~1 m above the seafloor and manually closed. In total, seven depths were sampled at every station. The shallowest sample on each cast was collected at ~2 m depth and is hereafter referred to as the “surface” sample.

The water sample temperature, salinity, and O_2 data were all taken from the Sea-Bird Electronics CTD rosette data corresponding to the time the bottle was closed. The temperature, salinity, and O_2 data for each near-bottom sample are taken from the CTD data matching with the deepest bottle closed on the corresponding rosette cast. Although a CTD and O_2 sensor attached to a frame without a rosette was deployed by hand to obtain a reading nearer to the bottom, the CTD frame stirred up sediment as it approached the seafloor, leading to erroneous salinity readings and making this method unreliable. O_2 was calibrated as described in section 2.3 and the other CTD sensors used the manufacturer's calibration.

2.2 CH_4 and N_2O sample collection and analysis

Water samples for CH_4 and N_2O analysis (duplicates for each depth) were collected into 120 mL glass serum bottles using flexible PVC tubing, with a volume of at least three times the sample volume flowing through the bottle before the sample was sealed. Samples were preserved following published procedures: 0.5 mL of 8 M potassium hydroxide (KOH) was used in August (Magen et al., 2014) and 100 µL of 3.8 g L^{-1} mercuric chloride solution (approximately 50% saturation) was used in October and May (Dickson et al., 2007). Experiments in our lab have demonstrated that these two preservation methods yield statistically equivalent and stable concentrations for CH_4 and N_2O over storage periods from 0 to 4 months (results for 6 months are pending analysis; manuscript in preparation). Samples were sealed with bromobutyl rubber stoppers and aluminum crimp seals. Analysis was completed within 5 months of each cruise.

Samples were prepared for analysis using headspace equilibration (Magen et al., 2014; de la Paz et al., 2021). Briefly, ~22 mL of water sample was removed while ~22 mL of ultrahigh purity N_2 (5.0 grade) at ambient atmospheric pressure was added. The samples were shaken for approximately 3 hours at room temperature. Then, approximately 20 mL of the headspace was transferred to a 12 mL pre-evacuated vial (Labco Exetainer) by injecting ~20 mL of brine solution (105 mg L^{-1} NaCl) into the bottom of the sample bottle and inserting a needle into the headspace to transfer the headspace gas into the vial. The Exetainer was filled to >1 atm pressure to prevent air from entering the vial when the needle was removed. The Exetainers contained dried KOH to remove CO_2, which can interfere with the quantification of N_2O (Zheng et al., 2008).

Samples were analyzed using an SRI 8610C gas chromatograph with flame ionization detector (FID) for CH_4 and electron capture detector (ECD) for N_2O. An xyzTek Bandolero autosampler was used to transfer the sample into two loops in sequence, with a 2 mL loop going to the FID and 0.25 mL loop going to the ECD. The sample loop and autosampler tubing was evacuated to below 6 torr, and then a needle was injected into the Exetainer vial, allowing the sample gas to fill the evacuated loops. The injected gas in the sample loop equilibrated to atmospheric pressure prior to transfer to the column. The FID flow path included a HayeSep D pre-column followed by a Shincarbon column to optimize separation of O_2 and CH_4. For the ECD, there was a HayeSep D pre-column followed by two HayeSep D columns with a vent in between to prevent O_2 from reaching the detector. Backflushing the pre-columns prevented water vapor from entering the main separatory columns. The carrier gas for the FID was N_2 with hydrogen gas (H_2) added to generate the flame, and for the ECD it was N_2 with P5 (95% methane, 5% argon) added as makeup gas at the detector to increase sensitivity.

Samples were calibrated using a standard containing 9.82 ppm CH_4 and 7.97 ppm N_2O in N_2. The certified standard was obtained from Airgas and calibrated internally using an air standard from the NOAA Carbon Cycles and Greenhouse Gas Group (Boulder, Colorado, USA) to reference all data to the WMO scale (Dlugokencky et al., 2020a, b) with an accuracy of 1% for both CH_4 and N_2O. For each set of water samples run, a set of seven standards ranging from 0 ppm to 9.82 ppm CH_4 and 0 to 7.97 ppm N_2O was prepared by mixing the Airgas standard with pure N_2 using Alicat mass flow controllers and injecting each standard mixture into Exetainer. A linear calibration curve was used for CH_4 and a quadratic calibration curve was used for N_2O (Wilson et al., 2018).

As part of every sample run, samples of deionized water equilibrated at room temperature (~22 °C) were collected and analyzed following the protocols described above. Community reference materials for CH_4 and N_2O in water are not commercially available, and therefore, preparation of air-equilibrated water samples in house is currently recommended as a quality assurance measure (Wilson et al., 2018). Compared to expected results based on atmospheric gas concentrations in Mashpee, Massachusetts, USA (see section 2.4), the average error for these samples was 0.32 nmol kg^{-1} for CH_4 and 0.07 nmol kg^{-1} for N_2O. The median precision of duplicate field samples was 4 nmol kg^{-1} (7% relative standard deviation) for CH_4 and 0.3 nmol kg^{-1} (3% relative standard deviation) for N_2O.

2.3 O_2 sample collection and analysis and correction of in situ O_2 data

To calibrate the SBE 43 O_2 sensor on the rosette, discrete samples for O_2 concentration measurement were collected on several casts on each cruise. Water samples were collected into 140 mL glass biological oxygen demand (BOD) flasks with flared necks using flexible PVC tubing, with at least three times the sample volume flowing through the bottle before the sample was sealed.

O_2 samples were preserved by adding 1 mL of $MnCl_2$ solution and 1 mL of NaI-NaOH solution before inserting a ground glass stopper (Langdon, 2010). The flared neck was filled with water, and the neck and stopper were covered with a latex rubber seal to keep the stopper in place and reduce evaporation. Samples were stored in the dark prior to analysis, which occurred within a few days of each cruise. Analysis was performed via amperometric Winkler titration with a precision of ~0.3% based on the standard deviation of duplicate samples (Langdon, 2010). Due to the slow response time (hysteresis) of the SBE43 O_2 sensor (Bittig et al., 2018; Martini et al., 2007) and strong stratification in the system (the mixed layer depth averaged 5 m) we have visualized and archived the O_2 data using discrete measurements of O_2 from the upcast corresponding to the time when the bottle was closed. On the upcast, the sensor was held at a fixed depth for at least 30 seconds prior to closing each Niskin bottle. On the downcast, the profiler was moving at ~1 m/s and the measured O_2 values lagged the in situ values. The discrete O_2 sample data was used to apply a linear correction factor to the O_2 sensor data for each cruise.

2.4 Equilibrium concentrations and sea-air flux calculations

In this manuscript, we report the saturation anomaly, Δ, as the concentration or percentage over or undersaturation (depending on context). For O_2:

$$\Delta O_2, \mu\text{mol kg}^{-1} = [O_2]_{\text{meas}} - [O_2]_{\text{eq}} \quad (1)$$

$$\Delta O_2, \% = \frac{[O_2]_{\text{meas}} - [O_2]_{\text{eq}}}{[O_2]_{\text{eq}}} \times 100\% \quad (2)$$

Here $[O_2]_{meas}$ and $[O_2]_{eq}$ are the measured and equilibrium concentrations of O_2, respectively. Equilibrium concentrations were calculated from the measured temperature and salinity following Wiesenburg and Guinasso (1979) for CH_4 and Weiss and Price (1980) for N_2O using MATLAB functions by Manning and Nicholson (2022). All gas concentrations are reported in molal units (mol kg^{-1}) to allow the gases to be used as conservative tracers. This molal unit convention for the reporting of O_2 and other chemical concentrations in seawater is used by global oceanographic programs including the Global Ocean Ship-Based Hydrographic Investigations Program (GO-SHIP) and Biogeochemical Argo (Bittig et al., 2018; Thierry et al., 2025).

Sea-air gas flux was calculated for CH_4 as follows, and an analogous approach was used for N_2O

$$\mathrm{F} = \mathrm{k}\left([\mathrm{CH_4}]_{\mathrm{meas}} - [\mathrm{CH_4}]_{\mathrm{eq}}\right). \tag{3}$$

Here positive values indicate a net sea to air flux (i.e., outgassing), and *k* is the gas transfer velocity calculated with the equation of Wanninkhof et al. (2014), which is a function of the wind speed at 10 m height and the Schmidt number of the gas. Schmidt numbers for CH_4 are calculated based on Jähne et al. (1987) and Schmidt numbers for N_2O are calculated following Wanninkhof (2014), which uses coefficients based on prior publications by Hayduk and Laudie (1974) and Wilke and Chang (1955).

For calculating equilibrium concentrations, the dry atmospheric concentration of CH_4 was assumed to be 2020 ppbv and N_2O was assumed to be 338 ppbv. These concentrations are taken from preliminary surface flask results from Mashpee, Massachusetts, USA (station MSH) from the NOAA Carbon Cycle Greenhouse Gases group website (https://gml.noaa.gov/ccgg/) and represent the average over the three cruises (Dlugokencky et al., 1994, 2020b, a; Hall et al., 2007; Lan et al., 2021). Final surface flask results were not available at the time of submission, but small changes in the atmospheric concentration would have a negligible impact on the calculated sea-air fluxes, relative to other sources of error in the calculations (e.g., the 20% uncertainty in the parameterization of *k* as a function of wind speed). The dry atmospheric concentrations were adjusted to wet concentrations by assuming 100% relative humidity at the air-sea interface and adjusted to local sea level pressure using the mean sea level pressure from the 15 days prior to each measurement which was measured using a mooring at station EXRX, NOAA buoy 44022 (NDBC, 2025). Wind speed was measured on the same mooring and extrapolated from the measurement elevation of 3.5 m to 10 m following Hsu et al. (1994).

Gas transfer velocity is non-linear function of wind speed, i.e., higher wind speeds have a disproportionate effect on the total flux, and therefore gas fluxes calculated based on average wind speeds will underestimate the true flux and fluxes based on instantaneous wind speeds can be biased high or low (Wanninkhof et al., 2009). To account for variability in wind speeds, we determine fluxes using the weighted gas transfer velocity, *k*, calculated following the equation of Teeter et al. (2018), which is modified from Reuer et al. (2007).

$$k = \frac{\sum_{t=1}^{n} k_t\,\omega_t}{\sum_{t=1}^{n} \omega_t} \tag{4}$$

$$\omega_n = 1,\ \omega_i = \omega_{i+1}(1 - f_{i+1}) \tag{5}$$

$$f_i = \frac{k_i \Delta t}{MLD} \tag{6}$$

In equation 1, *t* is the time index, with *t* = *n* representing the time of sampling, and *t* = 1 occurring 15 days prior. The term k_t refers to the gas transfer velocity (m s^{-1}) at time step *t*, and ω_t is the weighting at index *t* (ranging from 0 to 1). The variable f_i is the fraction of the mixed layer ventilated at index *i*, ω_i is the weighting coefficient at index *i*, MLD is the mixed layer depth, and Δt is the time interval between each wind speed measurement (15 min in this study). We use a time interval of 15 min so that $f_i \leq 1$ at every time point, despite the shallow mixed layer depths. The weighting coefficient decreases going back in time, since it is the product of the current weighting coefficient and the previous weighting coefficient (always ≤ 1), and also decreases as the gas transfer velocity decreases.

The mixed layer depth was defined using CTD profiles that were averaged into 1 m depth bins, based on a density difference criterion of 0.125 kg m^{-3} relative to the nearest-surface bin (2–3 m). The mixed layer depth was assumed to be constant in time for the flux calculation. Mixed layer depths ranged from 3–14 m (median 5 m, mean 5.8 m).

Previous publications have discussed what time period should be used when performing weighted flux calculations; a shorter weighting is favored when the residence time of gases in the mixed layer is short (Teeter et al., 2018). Here, a weighting period of 15 days was selected because the mean residence time of both CH_4 and N_2O was 4 days. Additionally, the meteorological sensors on the buoy at EXRX malfunctioned beginning in September 2023 and were replaced 16 days prior to the October cruise. For this reason, a longer integration period in October was not possible. For May and August, where 30 days of wind speed data was available prior to the cruise, we compared the gas transfer velocities calculated using a weighting period of 15 and 30 days and found that they agreed within 3%.

Typical uncertainty in sea-air gas fluxes was estimated to be 24% for CH_4 and 26% for N_2O using a Monte Carlo error analysis that incorporated the largest known sources of uncertainty (quantified here as relative standard deviation): the parameterization of k as a function of wind speed, at 20% per Wanninkhof et al. (2014); the measured wind speed, at 3% per the manufacturer's specifications; and the gas concentration, at 12% for CH_4 and 4% for N_2O. The uncertainty in the gas concentrations is based on the relative standard deviation of repeat measurements at station MID4 collected over 8 profiles during each cruise; this reflects uncertainty in the fluxes driven by short-term variability in gas concentrations that was not captured by the instantaneous sampling. The uncertainty due to instantaneous sampling is greater than the analytical uncertainty (reproducibility of duplicates). One potential systematic error that is not captured in our error estimates is lateral variability in wind speed along the transect, which could not be quantified as wind speed data was only available at station EXRX.

3. Results and Discussion

3.1 Seasonal and spatial trends in hydrography

The sampling months were chosen to reflect the annual variability in hydrographic properties in western LIS, enabling investigation of how the dissolved gas concentrations varied along with these seasonal changes. We sampled in August 2023 (near the annual maximum extent of hypoxia), October 2023 (following seasonal ventilation of the subsurface), and May 2024 (near peak river inflow and prior to the onset of hypoxia). The temperature and salinity of the water sampled reflect progressive cooling and freshening of the water from August through May (O'Donnell et al., 2008). Specifically, in August, temperature ranged from 20.1 to 24.1 °C and salinity from 26.0 to 27.0 PSS, in October, temperature ranged from 17.0 to 18.1 °C and salinity from 24.7 to 26.5 PSS, and in May, temperature ranged from 11.4 to 17.9 °C and salinity ranged from 22.4 to 24.2 PSS (Figure 2). Our hydrographic data are consistent with prior observations, which showed the annual minimum salinity in LIS typically occurs in May and is associated with peak freshwater inputs from rivers (Lee and Lwiza, 2005; O'Donnell et al., 2014).

Using transect data at the depths sampled for gases, the in situ temperature, reported as mean (standard deviation) was 21.6 (0.9) °C in August, 17.4 (0.4) °C in October, and 13.6 (1.8) °C in May. Salinity was 26.63 (0.27) PSS in August, 25.71 (0.52) PSS in October, and 23.39 (0.49) PSS in May. October displayed the least stratification, and August displayed the strongest stratification and shallowest mixed layer depths (Figure 3j-l). In October, the stratification and thermal gradient reached a minimum, with surface waters typically displaying a lower temperature than the subsurface (mean surface temperature of 17.1 °C; and mean temperature below 10 m of 17.7 °C). Seasonal cooling due to changes in surface heat flux causes the decline in temperature and stratification over fall and winter (Lee and Lwiza, 2008; O'Donnell et al., 2014).

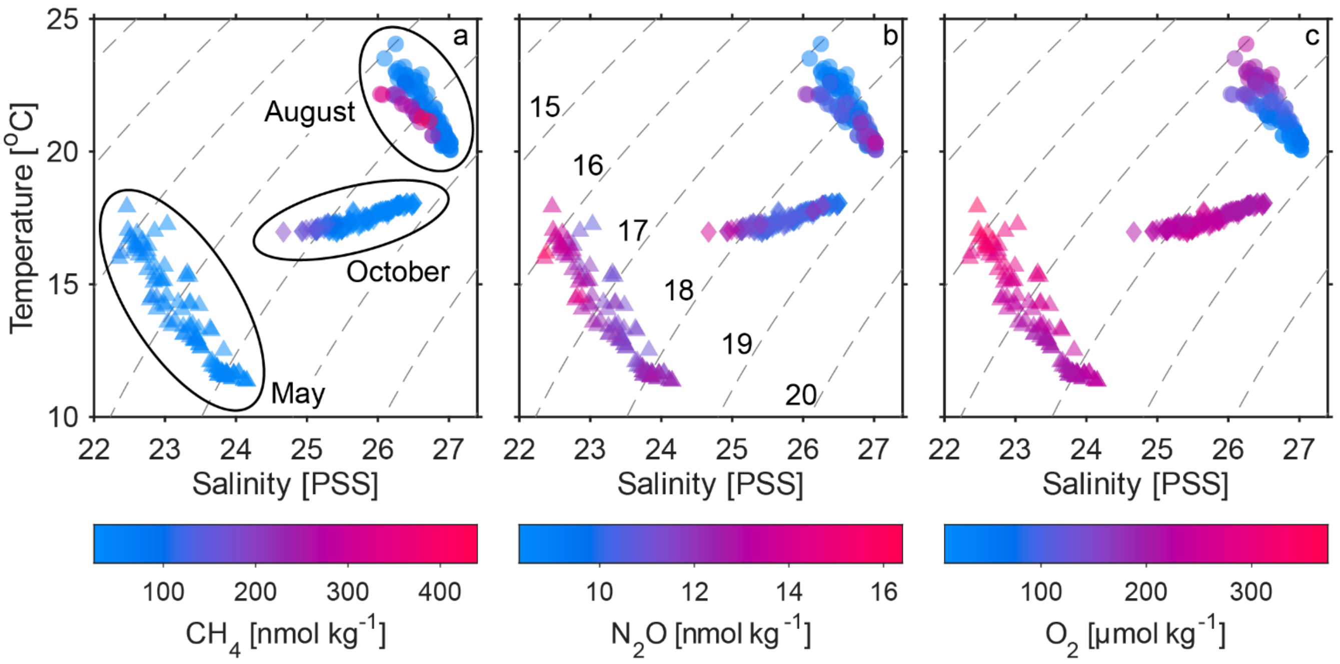

Figure 2. Temperature-salinity plot showing water mass distributions of CH_4, N_2O, and O_2 concentrations. CH_4 concentration (a), N_2O concentration (b) and O_2 concentration (c) during August (circles), October (diamonds) and May (triangles). In panel a, ellipses indicate the cluster of data points from each month. Dashed lines represent the density anomaly (kg m^{-3}), labelled in panel b. Here, all data from all stations are included, including repeat profiles at MID4 and EXRX.

Alt Text: Scatter plot of dissolved gas concentrations (CH_4, N_2O, and O_2) visualized as a function of temperature and salinity. The data show distinct water masses were present in each sampling month, with August showing the highest temperature.

Generally, density and salinity increased from west to east throughout the water column, consistent with prior observations and reflecting the influence of the low salinity waters discharged from the East River, a tidal strait between Manhattan and Long Island that connects LIS to New York Harbor and the Hudson River (Lee and Lwiza, 2005; O'Donnell et al., 2008). Within the East River, there is two-layer estuarine flow with net surface transport toward LIS and subsurface transport toward New York Harbor, though flow direction can temporarily reverse (Blumberg and Pritchard, 1997; Gay et al., 2004). Surface measurements (~2 m depth) in May displayed slightly less consistent trends along the transect (Figure 3l); although the westernmost station (EXR1) had the lowest salinity and density and the easternmost station (WLI6) had the highest salinity and density, the intermediate stations did not display a consistent east-west gradient in salinity and density. In particular, station EXRX displayed the highest surface density (16.8 kg m^{-3} at EXRX) compared to 16.0 kg m^{-3} at EXR1 to the west and 16.0 to 16.3 kg m^{-3} at the remaining stations to the east), suggesting the presence of a different mixed layer water mass at EXRX that was not present in the mixed layer at the other stations.

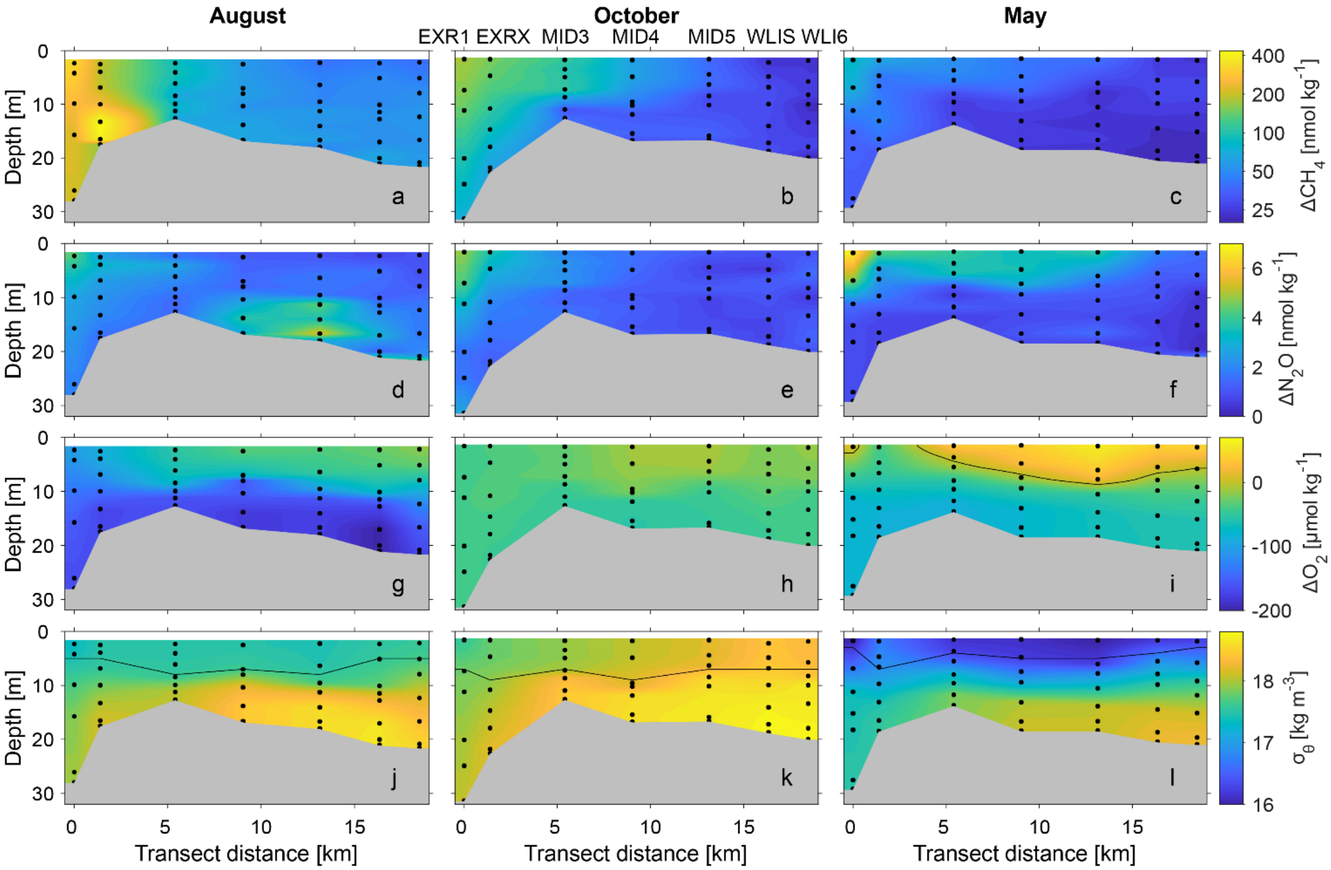

Figure 3. Measurements of CH_4, N_2O, O_2 and potential density anomaly collected along the 18 km transect in western LIS. The first three rows show gas saturation anomalies: ΔCH_4 in nmol kg^{-1} (a–c), ΔN_2O in nmol kg^{-1} (d–f), and ΔO_2 in μmol kg^{-1} (g–i). The bottom row is the potential density anomaly in kg m^{-3} (j-l). Note that ΔCH_4 is plotted using a logarithmic scale bar to better display the lateral gradients in each season. The black line on panel i represents equilibrium (ΔO_2 = 0 μmol kg^{-1}); O_2 was undersaturated at all stations along the transect in August and October. The sampling depths are indicated with black circles, and the station names are labelled above panel b. In the density plots (j–l), the solid line represents the mixed layer depth. Reference Figure 1 for the position of the transect.

Alt Text: Depth section contour plots of dissolved gas saturation anomalies (CH_4, N_2O, and O_2) and potential density anomaly measured in August, October, and May along the seven-station transect shown in Figure 1.

3.2 Seasonal and spatial trends in CH_4, N_2O, and O_2 along the transect in western LIS

Over the three cruises, along the entire transect and all depths, CH_4 concentrations ranged from 25–438 nmol kg^{-1} (840–18100 % saturation), N_2O concentrations ranged from 8.4–16.3 nmol kg^{-1} (102–173% saturation), and O_2 concentrations ranged from 8–372 μmol kg^{-1} (4–146% saturation) as reported in Table 1 and visualized in Figure 3a–i. Evaluating the entire transect, CH_4 concentrations and saturation anomalies were highest in August (mean 119 nmol kg^{-1}, 4900%) and lowest in May (mean 38 nmol kg^{-1}, 1200%). Mean N_2O concentrations were highest in May (mean 12.0 nmol kg^{-1}) and lowest in August (mean 10.1 nmol kg^{-1}), whilst the mean N_2O saturation anomaly was highest in August (mean 31 %) and similar in October and May (mean 19% in October and 18 % in May). Mean O_2 concentrations and saturation anomalies were lowest in August (mean 110 μmol kg^{-1}, −52%) and increased to similar levels in October (mean 220 μmol kg^{-1}, −13%) and May (mean 240 μmol kg^{-1}, −13%). However, O_2 was more homogeneous in October (the saturation anomaly had a standard deviation of 5% and O_2 was undersaturated at all depths), compared to May (the saturation anomaly had a standard deviation of 15% and reached a maximum of 24%), consistent with a less stratified water column (section 3.1).

Table 1. Temperature, salinity, and gas distributions incorporating measurements along the transect in western LIS from EXR1 to WLI6. Values in square brackets represent the first and third quartile and values in parentheses represent the standard deviation.

	August		October		May	
Parameter	Median	Mean	Median	Mean	Median	Mean
Temperature (°C)	21.4 [20.9, 22.3]	21.6 (0.9)	17.3 [17.1, 17.9]	17.4 (0.4)	13.3 [11.8, 15.2]	13.6 (1.8)
Salinity (PSS)	26.6 [26.4, 26.9]	26.6 (0.3)	25.6 [25.3, 26.2]	25.7 (0.5)	23.4 [23.0, 23.8]	23.4 (0.5)
CH_4 concentration (nmol kg^{-1})	68 [58, 194]	119 (101)	43 [32, 98]	67 (44)	32 [29, 45]	38 (13)
CH_4 saturation anomaly (%)	2700 [2300, 8100]	4900 (4200)	1500 [1200, 3600]	2400 (1600)	1000 [900, 1500]	1200 (500)
N_2O concentration (nmol kg^{-1})	9.8 [9.3 10.8]	10.1 (1.1)	10.2 [9.9, 11.0]	10.5 (1.0)	11.6 [11.4, 12.5]	12.0 (1.1)
N_2O saturation anomaly (%)	27 [21, 37]	31 (13)	16 [13, 22]	19 (10)	11 [8, 23]	18 (15)
O_2 concentration (µmol kg^{-1})	89 [69, 159]	110 (52)	217 [210, 231]	220 (14)	231 [211, 260]	240 (34)
O_2 saturation anomaly (%)	−62 [−71, −31]	−52 (23)	−14 [−16, −8]	−13 (5)	−19 [−26, −3]	−13 (15)

The clearest and most seasonally consistent spatial trend along the transect was that the concentrations of CH_4 and N_2O in the upper ~10 m were highest at the westernmost station, EXR1, and generally decreased eastward, and conversely, O_2 generally showed the opposite trend (Figure 3). These trends were observed in all three seasons, despite seasonal changes in the gas concentration ranges. Lateral gradients in O_2 in LIS and more severe O_2 depletion in the far western reaches of LIS are both annual features of the O_2 dynamics in LIS (O'Donnell et al., 2014; Whitney and Vlahos, 2021). One exception to this trend is in May 2024 where the westernmost station EXR1 had a higher surface O_2 concentration compared to the adjacent station EXRX (276 µmol kg^{-1} at EXR1 compared to 233 µmol kg^{-1} at EXRX). The remaining stations in this transect, to the east of EXRX, had higher and similar O_2 concentrations (290 to 323 µmol kg^{-1}). However, the CH_4 and N_2O concentrations at EXR1 and EXRX followed the expected west-east gradient in May (i.e., EXR1 displayed the highest surface concentrations of CH_4 and N_2O). As discussed in section 3.1, the surface potential density anomaly at EXRX was significantly higher than at any other station in the transect.

Although O_2 decreased with depth at each station in the transect in all three months (i.e., the bottom water O_2 concentration was always lower than the surface concentration), the vertical gradients in CH_4 and N_2O were more variable. In October and May, five to seven of the seven transect stations had higher CH_4 and N_2O concentrations at the surface compared to the bottom. In August some stations had both surface and subsurface CH_4 and N_2O peaks and the positions of CH_4 and N_2O maxima were notably not coincident. The easternmost stations WLIS and WLI6 consistently displayed the lowest surface CH_4 and N_2O concentrations and the smallest vertical ranges in CH_4 concentration. Comparing CH_4 and N_2O, CH_4 displayed a larger range in concentration and saturation anomaly across the entire transect as well as a larger range in concentration and saturation anomaly at individual stations on each cruise.

The transect measurements shown in Figure 3 were collected over a ~6 h period on each cruise beginning near 08:00 local time and therefore the spatial trends observed were influenced to some extent by differences in tidal phase and diel variability in biological processes. For the transect as a whole, we are unable to evaluate the contribution of temporal differences to the observed spatial trends, given that we only collected one profile at five of the seven stations on each cruise. However, the consistent patterns observed across all three months of an enrichment in near-surface CH_4 and N_2O concentrations at the westernmost station (with concentrations decreasing eastward) and depletion in near-surface O_2 concentrations at the westernmost station (with concentrations increasing eastward) gives us confidence that these are persistent features of the system. In section 3.3 we investigate the diel variability at station MID4.

3.3 Diel variability in CH_4, N_2O, and O_2 observed in repeat measurements at MID4

We sampled at station MID4 eight times on each cruise, every ~4 hours beginning near 08:00 on day 1 (Figure 4). From these data, we aimed to characterize temporal evolution in CH_4, N_2O, and O_2 on sub-daily timescales. Tides in LIS are semidiurnal and display significant spatial variability in timing and magnitude due to the bathymetric constrictions near New York City and the influence of river inflow at multiple points (Bennett et al., 2010; Duvall et al., 2024; McCardell et al., 2016). To identify the direction of water flow at MID4 during each cruise, we used tidal current speed predictions generated by NOAA for 3, 9, and 14 m depth at station LIS1035 (200 m from MID4, Figure 1). NOAA researchers validated the current prediction model for this location through comparison to in situ observations, which showed a mean error of 8 minutes or less in the timing of flood, slack and ebb, and current speed root mean square error of 0.04 m s^{-1} (NOAA, 2025). The current predictions at both depths indicate that at MID4 during flood tide (positive current speeds), the water flows toward the East River, with a mean flood current direction of ~233° at 3 m, ~244° at 9 m, and ~251° at 14 m. The timing of flood and ebb tides varied with depth; during our three sampling months, the peak flood tide occurred first at 3 m, ~18 min later at 9 m, and ~38 min later at 14 m (Figure 4a–c). To compare the concentrations at consistent depths over time, we applied a linear interpolation to the discrete sample data from each profile to estimate the gas concentrations at 3, 9, and 14 m, which matched the depths of the tidal current predictions.

The concentration of O_2 at MID4 varied with season, depth, and time of day. O_2 concentrations were highest in May (mean of 317 µmol kg^{-1} at 3 m and 212 µmol kg^{-1} at 14 m) and lowest in August (mean of 196 µmol kg^{-1} at 3 m and 49 µmol kg^{-1} at 14 m), matching the seasonal trends across all stations. The variability observed in O_2 at 3 m depth at MID4 over the ~28 h repeat sampling was largest in May (range of 87 µmol kg^{-1}, from 276 to 363 µmol kg^{-1}), intermediate in August (range of 37 µmol kg^{-1}, from 179 to 216 µmol kg^{-1}) and smallest in October (range of 27 µmol kg^{-1}, from 231 to 258 µmol kg^{-1}). These trends are consistent with the east-west range in O_2 observed along the transect at 3 m depth (Figure 3g-i), which was also largest in May (84 µmol kg^{-1}) and smallest in October (30 µmol kg^{-1}). The range in O_2 at MID4 observed in each month consistently decreased with depth. For example, the range in O_2 in May was 87 µmol kg^{-1} at 3 m depth, 54 µmol kg^{-1} at 9 m depth, and 13 µmol kg^{-1} at 14 m depth.

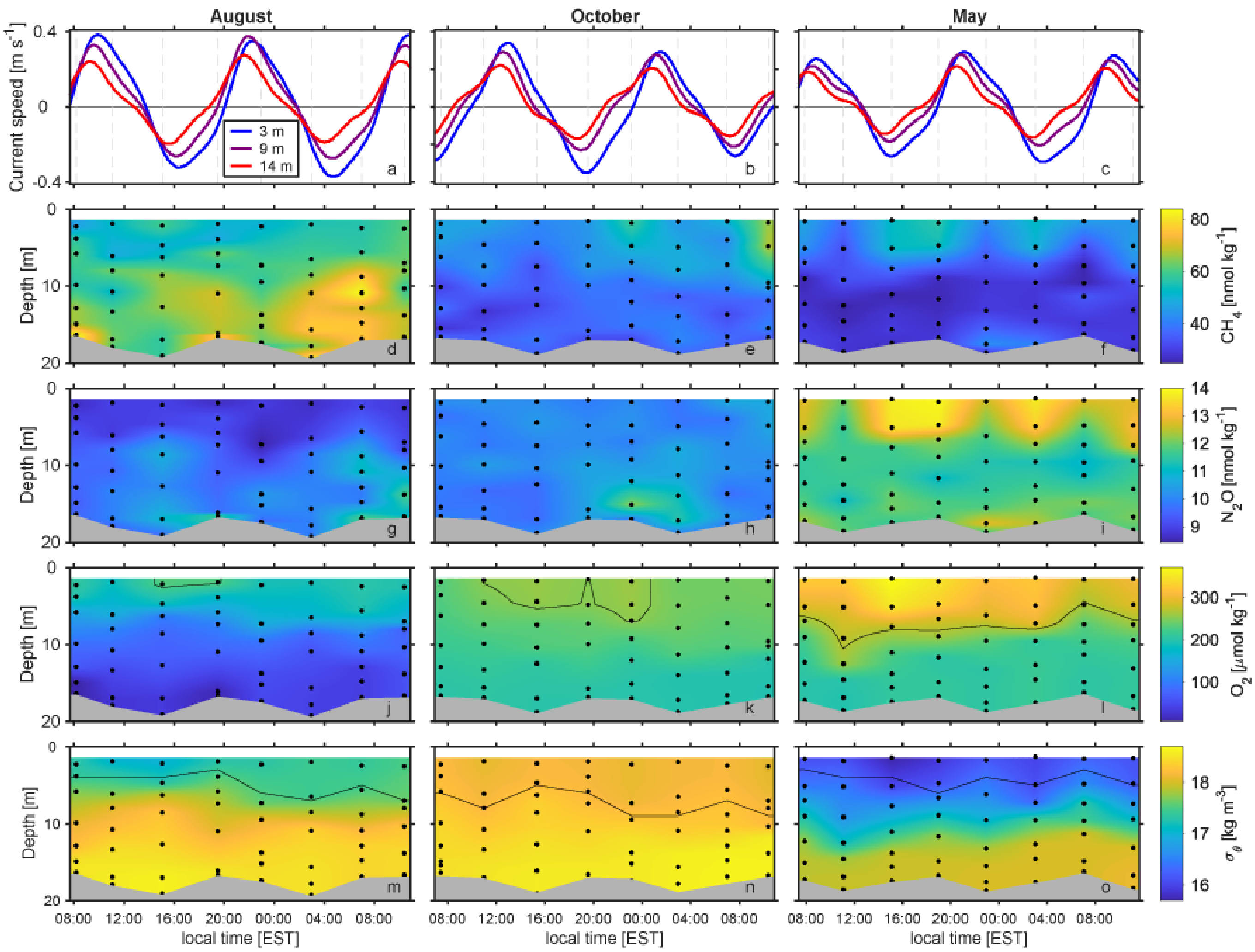

Figure 4. Time-series of repeat measurements at MID4 collected over ~28 h in each month. Predicted current speed in m s^{-1} at 3, 9, and 14 m depth at station LIS1035, near MID4 (a–c) on August 2-3, 2023 (a), October 19– 20, 2023 (b) and May 22-23, 2024 (c). Vertical dashed lines indicate sampling times. Here, positive current speeds indicate flow toward the southwest (flood tide, increasing water depth). Dissolved gas concentrations in samples collected at station MID4 over a ~28 h period: CH_4 in nmol kg^{-1} (d–f), N_2O in nmol kg^{-1} (g–i), O_2 in µmol kg^{-1} (j–l), and potential density anomaly in kg m^{-3} (m–o). Black circles indicate sampling times and depths. Measured bottom depth is variable due to the ~2 m tidal range at this site. In the O_2 plots (j–l), the solid black line represents equilibrium (depths above the line are supersaturated), and in the density plots (m–o) the solid line represents the mixed layer depth.

Alt Text: Top panel displays predicted current speeds in August, October, and May at stations LIS 1035, with a range of approximately −0.4 to 0.4 m s^{-1}. Lower panels display timeseries of CH_4, N_2O, and O_2 concentrations and potential density anomaly at station MID4.

At MID4, CH_4 and N_2O displayed different seasonal and daily trends from O_2 (Figure 4). CH_4 concentrations were highest in August (mean of 55, 64, and 68 nmol kg^{-1} at 3, 9, and 14 m depth, respectively) and lowest in May (mean of 46, 30, and 29 nmol kg^{-1} at 3, 9, and 14 m depth, respectively). Conversely, N_2O concentrations were highest in May (12.9, 11.6, and 11.7 nmol kg^{-1} at 3, 9, and 14 m depth, respectively), and lowest in August (8.9, 9.9, and 10.2 nmol kg^{-1} at 3, 9, and 14 m depth, respectively). For both gases, the seasonal trends at MID4 are consistent with the seasonal trends across the entire transect (Table 1). For each of the three depths evaluated, in each of the three months, the CH_4 concentration at MID4 varied by 6 to 25 nmol kg^{-1} over 28 h, and the N_2O concentration varied by 0.4 to 2.2 nmol kg^{-1} over 28 hr. Unlike for O_2, we did not observe a consistent decrease in the variability of CH_4 and N_2O with depth in each month. In October and May, the variability in CH_4 at MID4 over 28 h was largest at 3 m depth (20–25 nmol kg^{-1}) and smallest at 14 m depth (6–10 nmol kg^{-1}), which was consistent with the trends across the entire transect, and consistent with the trends observed for O_2. However, in August the 28-h CH_4 variability at MID4 was largest at 9 m depth (20 nmol kg^{-1}) and smallest at 3 m depth (12 nmol kg^{-1}), even though over the seven-station transect the variability was largest at 3 m depth (290 nmol kg^{-1}) and smallest at 14 m depth (56 nmol kg^{-1}). Similarly, for N_2O, the 28-h variability at MID4 was largest at 14 m depth in August and October (2.0–2.2 nmol kg^{-1}) and largest at 3 m depth in May (2.0 nmol kg^{-1}), whereas the variability along the entire transect was largest at 3 m in all three months (3.3–5.3 nmol kg^{-1}). In section 3.4, we discuss how short-term variability in near-surface gas concentrations at MID4 influences the calculated sea-air fluxes.

To further evaluate the influence of diel changes in light and tidal stage on the dissolved gas data, we visualized the eight profiles relative to the time of local solar noon (approximately 13:00, varying by month) and relative to tidal phase (peak flood tide). For the sunlight-related analyses we defined solar noon as 0 h and then calculated the time of every profile relative to solar noon (Figure 5). From biological processes alone, we would expect near-surface O_2 to be highest near sunset due to the accumulation of photosynthetic O_2 during the day, and lowest near sunrise, due to the lack of photosynthesis and continued respiratory consumption overnight (Izett et al., 2024; Nicholson et al., 2015). At 3 m depth, the minimum O_2 concentration in October (231 μmol kg^{-1}) and May (276 μmol kg^{-1}) occurred in the sample collected closest to sunrise, as would be expected for a biologically dominated diel signal. However, in August, the minimum O_2 concentration (179 μmol kg^{-1}) occurred at 2 h before solar noon, with three profiles collected earlier in the morning but after sunrise showing a higher O_2 concentration (193–204 μmol kg^{-1}). In all three months, the maximum O_2 concentration at 3 m depth occurred 2–3 hours after local solar noon, and in all cases, there was a profile collected closer to sunset with a lower O_2 concentration at 3 m. Thus, our sampling at 4 h resolution suggests that the variability in near-surface O_2 may be influenced by diel changes in photosynthesis as well as physical factors. As discussed above, the daily range in O_2 was smaller at 9 and 14 m as compared to 3 m, making it more difficult to identify a daily cycle at these depths. Because photosynthetic O_2 production will not occur below the euphotic zone, these deeper depths would be less influenced by diel changes in biological production.

There is potential for diel variability in light to affect CH_4 and N_2O concentrations, but the expected light-driven cycle for these gases in western LIS was not known a priori, given that the relative importance of different sources and sinks was unknown. For example, nitrification rates are inhibited by light and enhanced by increases in NH_4^+ availability, which can vary daily due to changes in phytoplankton demand (Proctor et al., 2023; Smith et al., 2014). Other studies indicate that both CH_4 and N_2O can be produced in surface waters through photochemical reactions (Leon-Palmero et al., 2025; Li et al., 2020; Tang et al., 2014). Overall, we did not observe any consistent relationships between the stage of the solar cycle and the CH_4 and N_2O concentrations at 3, 9 and 14 m. Focusing on 3 m depth where the largest daily variability in light is observed, the minimum CH_4 concentration over 28 h of sampling occurred at 6.5, 2.7, and −1.8 h relative to solar noon in August, October, and May, respectively, while the maximum CH_4 concentration occurred at −2.6, −2.3, and 6.1 h relative to local solar noon in August, October, and May, respectively. At 3 m depth, the minimum N_2O concentration occurred at −10.1, −9.7 and −1.8 h relative to local solar noon in August, October and May, respectively, while the maximum N_2O concentration occurred at −6.0, −2.3, and 6.1 h relative to local solar noon in August, October, and May, respectively. For the deeper depths, there was similarly a lack of consistent relationship with time of day. As with O_2, we would expect the gas concentrations at 9 and 14 m depth to be less influenced by light variability due to the lower light levels available at these depths during daytime. We conclude that light variability is not the primary driver of daily variability in CH_4 and N_2O at MID4.

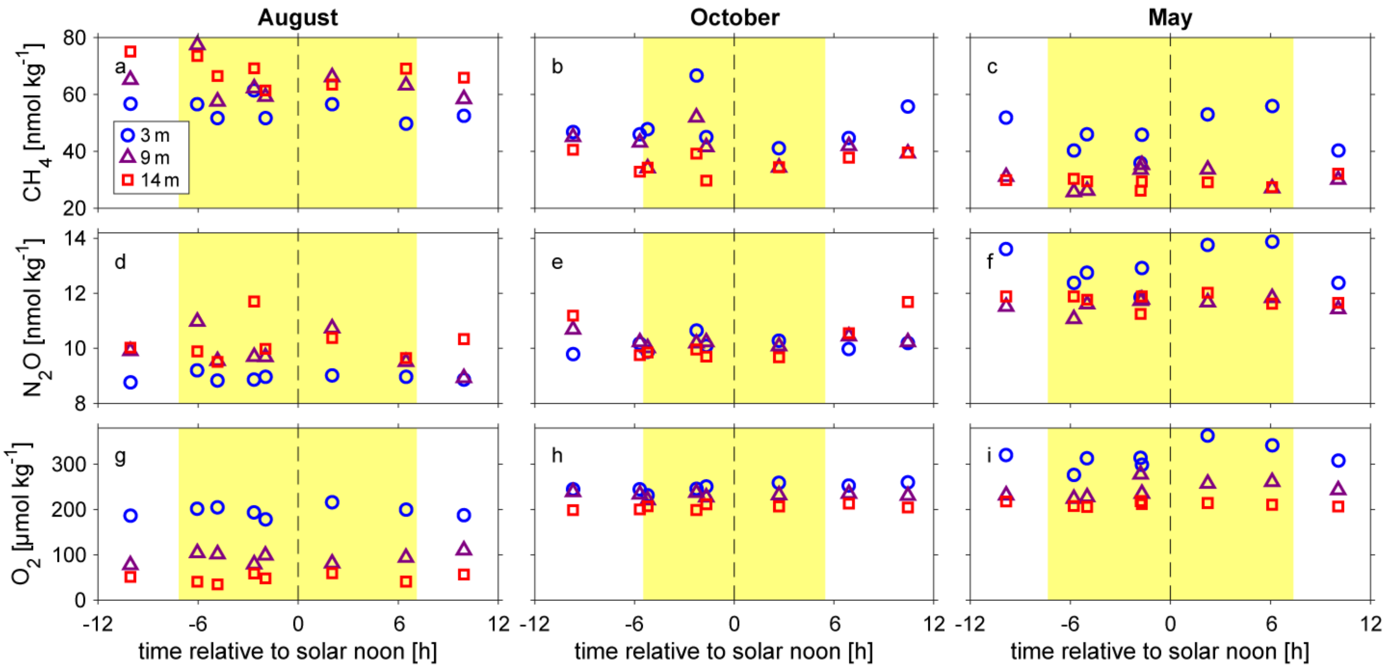

Figure 5. Dissolved gas concentrations measured at MID4 relative to the timing of solar noon. Concentrations of CH_4 in nmol kg^{-1} (a–c), N_2O in nmol kg^{-1} (d–f) and O_2 in µmol kg^{-1} (g–i) in August (left), October (center) and May (right column). Blue circles, purple triangles, and red squares represent 3, 9, and 14 m depth, respectively. The yellow shaded area is the period from sunrise to sunset.

Alt Text: Timeseries of dissolved gas concentrations (CH_4, N_2O, and O_2) at station MID4 for each cruise, visualized as a function of time relative to solar noon.

We further evaluated the gas time-series relative to tidal phase. In these visualizations, we defined the peak flood tide (maximum positive current speed in each tidal cycle) as 0 h and then calculated the time of each profile relative to the peak flood (Figure 6). Given the semidiurnal tides at this site, peak ebb will occur at approximately −6.2 h and 6.2 h relative to peak flood. As discussed in section 3.3, we observed that CH_4 and N_2O concentrations in the upper 10 m were highest in the westernmost station and generally decreased eastward, whereas O_2 had the opposite trend. Therefore, if the observed variability in gas concentrations was predominantly driven by tidal advection, we would expect CH_4 and N_2O concentrations at 3 m to be lower (and O_2 higher) during periods when water at MID4 had originated from the northeastern sound, i.e., near the end of the flood current (approximately 3.1 h relative to peak flood), and for CH_4 and N_2O concentrations to be higher (and O_2 lower) near the end of the ebb current (approximately −3.1 h relative to peak flood)

At 3 m depth, the minimum O_2 concentration occurred at 1.2, −5.5, and −2.4 h relative to peak flood, and the maximum concentration occurred at 5.2, −2.4, and −6.0 h relative to peak flood in August, October and May, respectively. Thus, only the timing of the minimum concentration in May followed the expected trend for an advection-dominated signal (minimum concentration ~3 h prior to peak flood). The influence of tidal cycles on O_2 in western LIS has been previously reported. For example, studies using continuous mooring data in western LIS reported that semidiurnal variability in near-bottom water O_2 levels are correlated with tidal activity and that tides contribute to both vertical and lateral O_2 transport. In summer, flood tides result in vertical transport of well-oxygenated water deeper in the water column, increasing near-bottom O_2 (Duvall et al., 2024; McCardell et al., 2016). However, at 14 m depth, we again did not see a consistent relationship between tidal phase and O_2 concentrations; the maximum O_2 concentration occurred at 5.8, −5.3, and 2.9 h relative to peak flood tide in August, May, and October, respectively, i.e., the summertime subsurface O_2 concentration was highest near peak ebb.

At 3 m, the maximum concentrations of both CH_4 and N_2O occurred at −3.4 h relative to peak flood in October, and −2.1 h relative to peak flood in May. In August, the maximum CH_4 concentration at 3 m occurred at −0.4 h relative to peak flood and the maximum N_2O concentration occurred at −3.8 h relative to peak flood. Thus, the timing of all but the maximum CH_4 concentration in August were consistent with variability driven by tidal advection. This is notable because the east-west CH_4 gradient in surface waters was largest in August and therefore we might have expected August to display the largest sensitivity to tidal advection. The minimum concentrations of CH_4 and N_2O occurred between 1.4 to 2.4 h relative to peak flood in October and May. In August, the CH_4 minimum occurred at −2.8 h relative to peak flood and the N_2O minimum occurred at 4.7 h relative to peak flood. Therefore, the timing of the near-surface CH_4 and N_2O minima in October and May was consistent with a horizontal advection-dominated signal, but the timing in August was not. However, tidally driven vertical transport may also influence the observed concentrations. In August, CH_4 and N_2O concentrations at 14 m depth were consistently higher than concentrations at 3 m, while May and October showed the opposite trend. If vertical mixing was enhanced during flood tides, this could potentially decrease the subsurface CH_4 and N_2O concentrations in August and increase them in October and May. However, this tidally driven vertical transport also did not appear to be the dominant driver of variability. For example, in August, at 14 m depth, the minimum and maximum N_2O concentrations both occurred during the flood tide (at −1.1 and 0.3 h relative to peak flood, respectively), and in May at 14 m depth, the minimum and maximum CH_4 concentrations both occurred near the end of the flood tide, at 2.9 and 2.4 h after peak flood, respectively.

Our observations at MID4 suggest that the drivers of variability in CH_4, N_2O, and O_2 are complex and cannot be correlated to light levels or tidal phase alone. Similarly, Duvall et al. (2024) found that at station EXRX, O_2 was influenced by both the diel variability in photosynthesis rates and tides. Given the lower sampling frequency and duration of our observations at MID4 (every 4 h over 28 h) as compared to previous studies based on mooring observations (e.g., every 15 min over several weeks), we are unable to perform quantitative correlations between the gas concentration data and tidal phase (or light levels). Higher frequency measurements of CH_4 and N_2O over a longer duration would be facilitated by future improvements in sensor technologies to enable accurate in situ measurements of these gases at the observed concentrations in western LIS. The data presented here provide the first insights into the influence of tidal dynamics and light in western LIS on the distributions of CH_4 and N_2O.

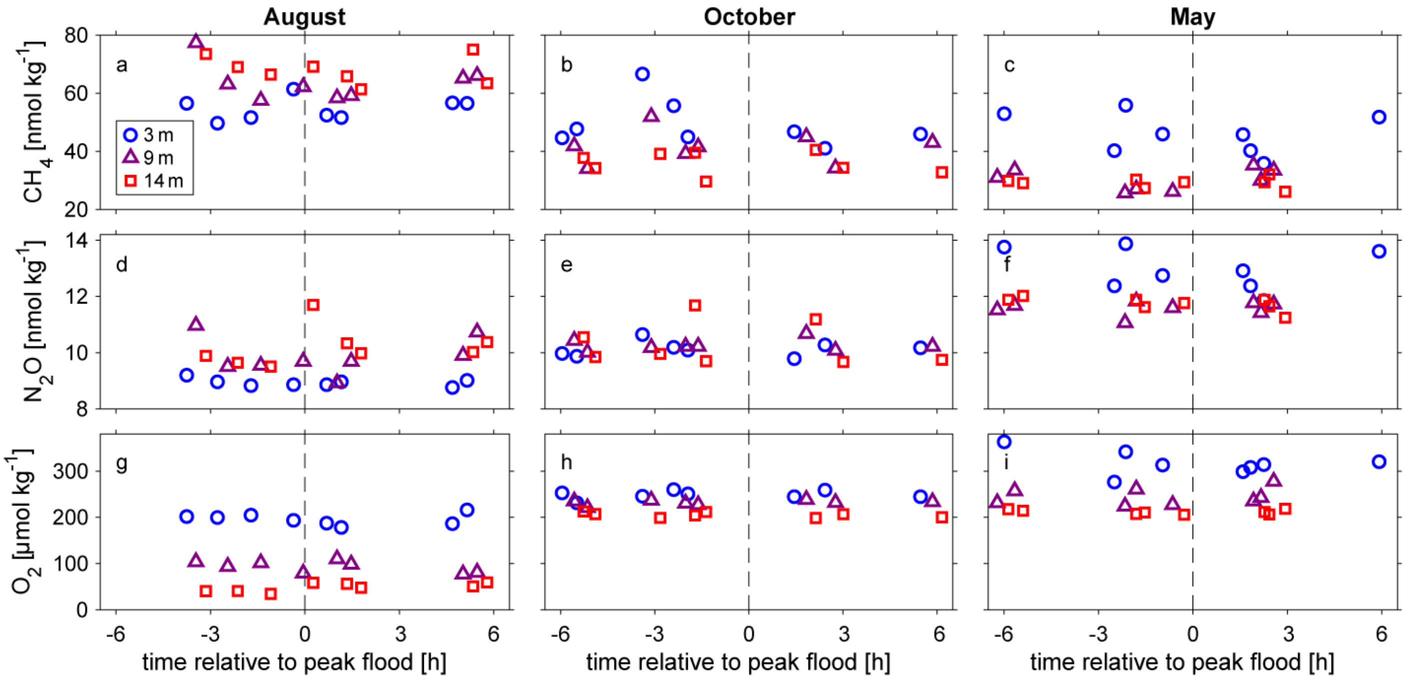

Figure 6. Dissolved gas concentrations at MID4 relative to the timing of peak flood. Concentrations of CH_4 in nmol kg^{-1} (a–c), N_2O in nmol kg^{-1} (d–f) and O_2 in µmol kg^{-1} (g–i) in August (left), October (center) and May (right column).

Alt Text: Timeseries of dissolved gas concentrations (CH_4, N_2O, and O_2) at station MID4 for each cruise, visualized as a function of time relative to solar noon.

3.4 Sea-air fluxes of CH_4 and N_2O

We calculated sea-air fluxes of CH_4 and N_2O at each station in each season following the procedures described in the Methods. In these calculations, the data from repeat stations were averaged to obtain one flux for each station in each month, to avoid over-weighting the stations that were sampled multiple times (EXRX and MID4). In all three months, the surface saturation anomalies, concentrations, and sea-air fluxes of both gases were highest at the westernmost station (EXR1) and followed a general decrease toward the east (Figure 5 and Table 2). Using the 15-day weighting method across the seven stations, the mean sea-air CH_4 fluxes (µmol m^{-2} d^{-1}) were 154 in August, 133 in October, and 62 in May, and the mean sea-air N_2O fluxes (µmol m^{-2} d^{-1}) were 2.5 in August, 3.3 in October, and 4.8 in May. Thus, the CH_4 fluxes were highest in August, whereas N_2O fluxes were highest in May.

Seasonal changes in gas transfer velocity and gas concentrations both influenced the sea-air fluxes of CH_4 and N_2O. The 15-day weighted CH_4 gas transfer velocity averaged 1.4 m d^{-1} in August, 1.6 m d^{-1} in October, and 1.3 m d^{-1} in May, and the weighted N_2O gas transfer velocity averaged 1.4 m d^{-1} in August, 1.5 m d^{-1} in October, and 1.2 m d^{-1} in May. Seasonal variability in wind speed (highest in October, increasing the gas transfer velocity) as well as changes in water temperature (highest in August, increasing the gas diffusivity and by extension the gas transfer velocity) drove these changes. Surface CH_4 saturation anomalies and concentrations were highest in August at every station except MID3, which had the highest concentration and saturation anomaly in October (Figure 5). The mean August surface CH_4 concentration was 90 nmol kg^{-1} and mean August surface CH_4 saturation anomaly was 4700% across the seven stations. Correspondingly, August had the highest sea-air flux because the mean CH_4 surface saturation anomaly was ~52% higher in August compared to October, even though the gas transfer velocity was ~13% lower in August compared to October.

The surface N_2O concentration and saturation anomaly was highest for N_2O in May at every station (mean concentration 13 nmol kg^{-1}, mean saturation anomaly 42%), leading to enhanced fluxes in May (Table 2).

To estimate annual mean and median fluxes and surface concentrations, we used the weighted flux and concentration data from August, October, and May and applied a linear interpolation at daily frequency over 1 year. We estimated the annual CH_4 flux to have a mean of 106 μmol m^{-2} d^{-1} and a median of 66 μmol m^{-2} d^{-1} and the annual N_2O flux to have a mean of 3.7 μmol m^{-2} d^{-1} and a median of 3.2 μmol m^{-2} d^{-1}. We estimated the surface CH_4 concentration to have an annual mean of 78 nmol kg^{-1} and a median of 50 nmol kg^{-1}, and the surface N_2O concentration to have an annual mean of 11.5 nmol kg^{-1} and a median of 11.1 nmol kg^{-1}. This approach has some uncertainty, because we did not collect data during November–April, and we did not utilize wind speed data outside of the 15 days prior to each cruise; due to gaps in the mooring wind speed data, we were not able to utilize a continuous 12-month timeseries of wind overlapping with our sampling dates. Nevertheless, it provides an initial annual estimate for comparison with results from other estuaries worldwide (section 3.8).

Finally, we evaluated the effect of the sampling time (e.g., due to daily variability in gas concentrations) on the calculated sea-air fluxes. For station MID4, which was sampled eight times on each cruise, the relative standard deviation of the 15-day weighted CH_4 flux from the 8 time points was 12%, 20%, and 21% in August, October, and May, respectively. The relative standard deviation of the 15-day weighted N_2O flux was 14%, 32%, and 28% in August, October, and May, respectively. The variability in sea-air fluxes was primarily driven by concentration changes, as the 15-day weighted gas transfer velocity for both gases had a standard deviation of 4% in August and October and 10% in May using all surface MID4 measurements. Instantaneous sea-air fluxes showed much stronger variability on sampling time. For example, the relative standard deviation of the instantaneous gas flux in May was 135% for CH_4 and 113% for N_2O due to large changes in wind speed during this cruise. This result demonstrates the advantage of using weighted gas fluxes, which account for variability in wind speed.

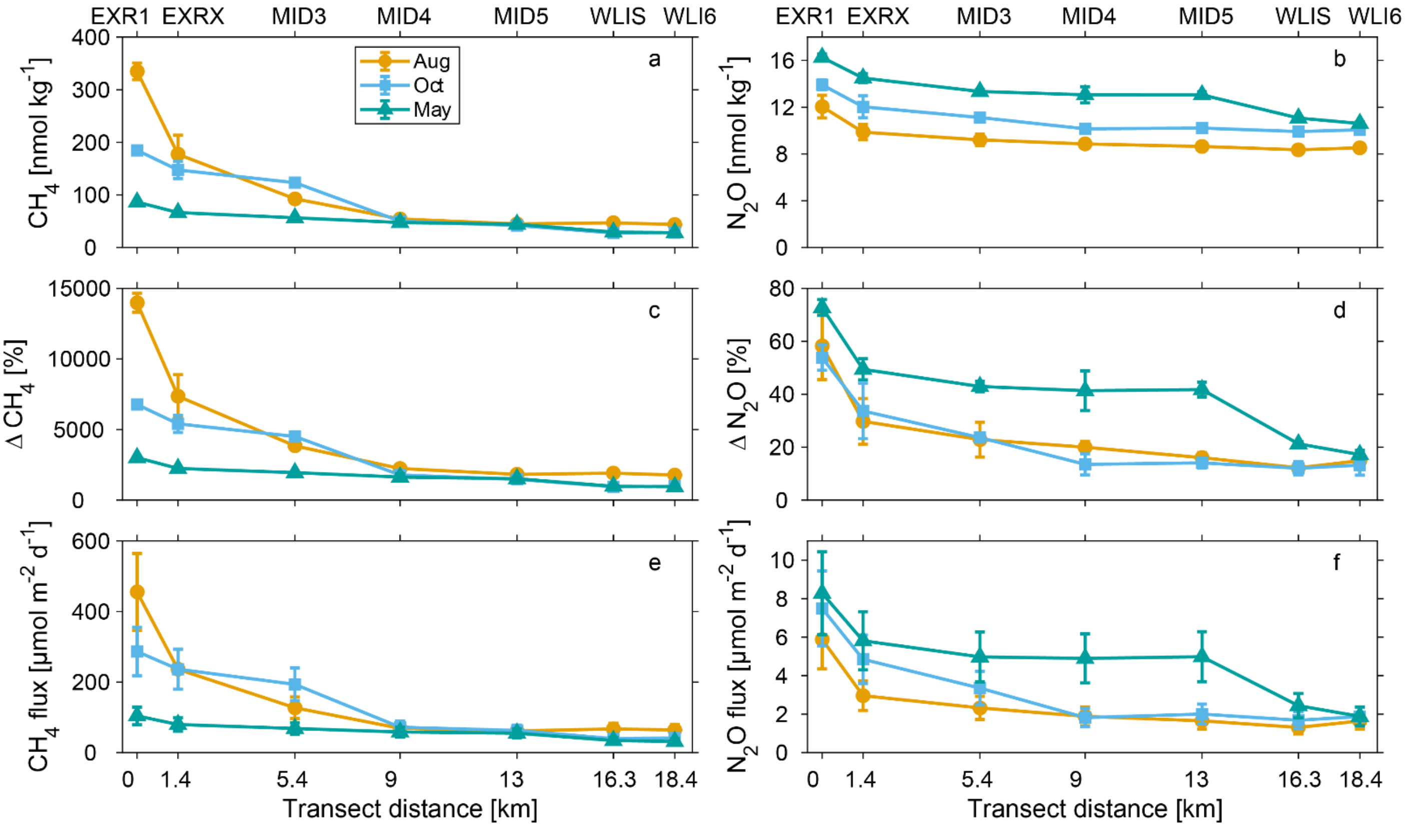

Figure 7. Surface concentrations, surface saturation anomalies and sea-air fluxes of CH_4 and N_2O. Surface concentrations (nmol kg^{-1}) of CH_4 (a) and N_2O (b), saturation anomalies (%) of CH_4 (c) and N_2O (d), and sea-air fluxes (μmol m^{-2} d^{-1}) of CH_4 (e) and N_2O (f) calculated using a 15-day weighting period for each of the seven stations. The transect distance corresponds to the position of each station along the transect, following Figure 1.

Alt Text: Surface CH_4 and N_2O concentrations, saturation anomalies, and sea-air fluxes. The data show that fluxes and concentrations generally decrease eastward, and that CH_4 fluxes are highest at EXR1 in August whereas N_2O fluxes were highest at EXR1 in May.

Table 2. Sea-air fluxes, surface concentrations, and surface saturation anomalies from all seven stations calculated using 15-day weighting scheme. For medians, values in curly brackets represent the minimum and maximum. For means, values in parentheses represent the standard deviation.

	August		October		May	
Parameter	Median {min, max}	Mean (std.)	Median {min, max}	Mean (std.)	Median {min, max}	Mean (std.)
CH_4 flux (μmol m^{-2} d^{-1})	69 {61, 455}	154 (147)	72 {40, 287}	133 (103)	59 {31, 104}	62 (25)
CH_4 surface concentration (nmol kg^{-1})	54 {44, 335}	114 (109)	50 {28, 185}	86 (64)	48 {28, 86}	51 (21)
CH_4 surface saturation anomaly (%)	2200 {1800, 14000}	4700 (4600)	1800 {900, 6800}	3100 (2400)	1600 {900, 3000}	1800 (700)
N_2O flux (μmol m^{-2} d^{-1})	1.9 {1.3, 5.9}	2.5 (1.6)	2.0 {1.7, 7.5}	3.3 (2.2)	5.0 {1.9, 8.3}	4.8 (2.1)
N_2O surface concentration (nmol kg^{-1})	8.9 {8.4, 12.1}	9.4 (1.3)	10.2 {9.9, 13.9}	11.1 (1.5)	13.1 {10.6, 16.3}	13.1 (1.9)
N_2O surface saturation anomaly (%)	20 {15, 28}	25 (16)	14 {12, 54}	23 (16)	42 {17, 73}	41 (18)

3.5 Potential sources and sinks of N_2O in western LIS

Although determining rates of specific N-cycling processes that influence N_2O is beyond the scope of this study, here we use the observed gas distributions and published literature on western LIS and the East River to speculate about potential N_2O sources and sinks and motivate future work. N_2O can be produced through both nitrification and denitrification. Water column nitrification rates in oxygenated systems typically increase with reduced competition for NH_4^+ from phytoplankton and decrease with increasing light levels, though different species of ammonia oxidizing archaea and bacteria exhibit different light sensitivities (Proctor et al., 2023; Smith et al., 2014; Ward, 2008).

The East River, which flows into western LIS, appears to have conditions primed for nitrification, and previous works have demonstrated its occurrence. Total ammonia (NH_4^+ + NH_3) concentrations are typically above 5 µmol L^{-1} (and can exceed 40 µmol L^{-1}), NO_2^- is typically above 2 µmol L^{-1} (and can exceed 10 µmol L^{-1}), and NO_3^- is typically above 2 µmol L^{-1} (and can exceed 30 µmol L^{-1}) (Gobler et al., 2006; Li et al., 2018). Comparing conditions in the East River and western LIS, salinity is lower, chlorophyll *a* concentrations are lower, and dissolved inorganic nitrogen (DIN) concentrations are higher in the East River (Bowman, 1977; Li et al., 2018; Wallace and Gobler, 2021), making the East River a net exporter of N to western LIS (Buck et al., 2005; Vlahos et al., 2020). These trends suggest that nitrifiers will experience reduced competition for NH_4^+ in the East River compared to western LIS due to the lower phytoplankton biomass and higher DIN. Euphotic zone depths in the East River are on the order of 4 m (reported range 1–8 m), indicating rapid attenuation of light, which is driven by suspended solids rather than phytoplankton biomass and may cause light limitation of phytoplankton growth in some seasons (Li et al., 2018). Somewhat deeper euphotic zone depths of 5–11 m have been reported for LIS (Anderson and Taylor, 2001; Goebel and Kremer, 2007). Nitrification has previously been reported in the East River from direct incubation measurements in the early 1970s (Chen et al., 1975). The authors found that nitrification rates increased when the salinity of the incubation water was decreased, suggesting nitrifying microbes in the East River are adapted to the fresh water released from the wastewater plants. This result suggests that the East River hosts a unique population of nitrifiers that would not be as active at the higher salinity levels observed in the water in western LIS. Additionally, recent research has proposed that nitrification significantly influences chemical concentrations in the East River (Wallace, 2020; Wallace and Gobler, 2021). Specifically, Wallace and Gobler (2021) estimated aerobic respiration-driven changes in pH and O_2 by collecting diurnal profiles from late afternoon to sunrise and found respiration rates to be lower in the East River than in western LIS. They concluded that aerobic respiration could not fully explain the biogeochemical conditions observed in the East River (low total alkalinity, low O_2, low pH, and high pCO_2) and proposed that ammonification of wastewater-derived organic N followed by nitrification could contribute to these observed conditions. It is also possible that sedimentary denitrification could contribute to the N_2O production in the East River given the high organic carbon supply. Due to rapid flushing and shallow bottom depths, the East River is not known to reach suboxic conditions in the water column (O'Connor, 1966). However, if denitrification in the East River were the primary driver, we would predict N_2O saturation anomalies to be highest later in the summer following more respiration within the system, rather than in early spring, the start of the productive season.

Overall, the highest N_2O concentration and saturation anomaly in our study was observed in the surface waters at station EXR1 in May, rather than in the stratified subsurface hypoxic waters of August, which we initially hypothesized would have the highest concentrations. Our observations of enhanced N_2O concentrations in the fresh water in the far western LIS suggest that either the N_2O is formed directly in the East River, or the substrates that lead to N_2O production are released from the East River and rapidly converted to N_2O within western LIS. Studies in other estuaries and rivers have reported elevated N_2O concentrations in wastewater effluent and/or downstream of some wastewater treatment plants, though results are highly variable (Burgos et al., 2015; Peterse et al., 2024; Tang et al., 2024b). Therefore, wastewater effluent may contribute to the elevated N_2O concentrations observed in the surface waters of western LIS.

We observed subsurface peaks in N_2O at the four easternmost stations in August and hypothesize that these trends reflect sedimentary sources, either from denitrification or nitrification. These elevated N_2O concentrations did not display a consistent relationship with O_2. Such a relationship, if observed, could suggest a dominant subsurface source from nitrification below the mixed layer (Nevison et al., 2003). The water column O_2 concentrations were consistently above the threshold for denitrification to occur, based on the minimum observed O_2 concentration in this study of 8 μmol kg^{-1} and an O_2 threshold ≤0.01 μmol kg^{-1} for denitrification (Zakem et al., 2020; Zakem and Follows, 2017). We therefore assume that active water column denitrification was not occurring at any of the times and locations we sampled. However, anoxic microenvironments within organisms, aggregates, and suspended/sinking particles may have provided sites for anaerobic metabolic processes to occur (Bianchi et al., 2018; Klawonn et al., 2015; Wan et al., 2023a, b). Mazur et al. (2021) performed sediment core incubations in LIS in summer and winter and found that sediments were on average a small net source of N_2O (mean 8.6 nmol N_2O m^{-2} h^{-1}) but sediment-water fluxes varied widely (range −32 to 68 nmol N_2O m^{-2} h^{-1}). Their incubations also demonstrated evidence of low and spatially variable denitrification rates based on net N_2 fluxes. These observations of spatial variability in sedimentary processes are consistent with our observed variability in the depth-dependent N_2O concentration gradient at adjacent stations with similar bottom-water O_2 concentrations.

3.6 Potential sources and sinks of CH_4 in western LIS

As for N_2O, determining the rate of CH_4 production and consumption is beyond the scope of this study. However, we can use the observed trends in CH_4 and the relationship between CH_4 and O_2 to speculate about potential sources and sinks and motivate future work. In the upper 10 m, CH_4 displayed the highest concentrations at the westernmost station (EXR1) during each cruise, and concentrations generally decreased eastward. We suspect that East River discharge influences near-surface CH_4 concentrations in western LIS, given the elevated concentrations in near-surface waters near the East River. Wastewater facilities are known to be significant sources of CH_4; the US EPA greenhouse gas inventory contains a category for CH_4 emissions from treated wastewater effluent (EPA, 2022). This category includes both CH_4 directly released from the wastewater facility and effluent and CH_4 production from the degradation of organic matter downstream of the facility (EPA, 2022). Studies of other wastewater facilities indicate that CH_4 concentrations can peak in wastewater effluent and/or downstream of wastewater plants (Alshboul et al., 2016; Jin et al., 2018; Peterse et al., 2024). Downstream peaks in CH_4 observed in other studies suggest internal production following discharge and may be associated with the high dissolved organic carbon (DOC) concentrations in wastewater effluent. In addition to having high DIN concentrations, the East River contains high DOC concentrations (~200 μmol kg^{-1}) (Buck et al., 2005), which may serve as a substrate for aerobic or anaerobic (sedimentary) CH_4 production, and photodegradation processes following release may increase the bioavailability of DOC (Yin et al., 2021; Yu et al., 2025). Although DOC concentrations are relatively uniform throughout the East River and LIS (Buck et al., 2005), the wastewater effluent-derived DOC present in the East River will have distinct chemical characteristics compared to the terrestrial-derived DOC and natural marine organic matter present farther east in the estuary, and this may affect the production rate of CH_4 from such DOC (Amaral et al., 2021; Gonsalves et al., 2011; Maya-Altamira et al., 2008).

In October and May, CH_4 concentrations were generally higher at the surface than in the subsurface. In August, some stations displayed CH_4 peaks at the surface and subsurface. For example, station EXRX displayed elevated subsurface concentration of CH_4 on August 3 (maximum of 438 nmol kg^{-1} at 16.5 m depth, compared to 203 nmol kg^{-1} at 2.5 m depth). The subsurface peaks could reflect local sedimentary production driven by organic matter diagenesis and diffusion and/or ebullition transporting CH_4 into the overlying water column (Bange et al., 2010; Valentine, 2011). Given the enhanced subsurface concentrations at EXRX and EXR1 relative to stations to the east, this sedimentary production could be occurring within western LIS or within the East River and be advected into the study area. Sedimentary effluxes of CH_4, particularly in the form of bubbles, can be strongly influenced by pressure, with lower pressure increasing gas efflux (Maeck et al., 2014; Nylund et al., 2025; Römer et al., 2016). Therefore, changes in tidal stage and overlying water depth may drive effluxes of gases and contribute to some of the spatial variability we observe in near-bottom waters for CH_4. Mazur et al. (2021) found using sediment core incubations that LIS sediments at stations EXRX and WLIS had on average net negative CH_4 fluxes in summer, though fluxes were widely variable with some cores showing strongly positive fluxes and others negative fluxes, and such sediment core incubations would not account for tidally-driven effluxes. As for N_2O, it is possible that we observed effects of transient CH_4 fluxes from the seafloor interacting with the effects of tidal advection causing transient near-bottom peaks in CH_4.

3.7 Role of CH_4 and N_2O in western LIS C and N budgets and global warming potential of emissions

We used the observed CH_4 and N_2O concentrations to assess their contribution to the overall C and N budgets for LIS. We conclude that CH_4 is not a significant contributor to the total C budget in western LIS: CH_4 concentrations in our study were ≤0.5 μmol kg^{-1}, whereas dissolved organic carbon concentrations typically exceed 100 μmol kg^{-1} and dissolved inorganic carbon concentrations typically exceed 1600 μmol kg^{-1} in this region (Barrett et al., 2024; Vlahos and Whitney, 2017). Similarly, N_2O is not a significant source or sink term in the total N budget for LIS. Dissolved N_2O concentrations did not exceed 0.016 μmol kg^{-1} in our study, whereas total inorganic N concentrations (excluding N_2 gas, which is not bioavailable to most organisms) in western LIS typically exceed 14 μmol kg^{-1} (Vlahos et al., 2020).

To contextualize the global warming impact of N_2O and CH_4 emissions from western LIS, we calculated their fluxes in units of CO_2-equivalents (CO_2e) and compared these values to estimated fluxes of CO_2, the anthropogenic greenhouse gas that is the biggest contributor to global warming (Forster et al., 2021). The global warming potential (GWP) quantifies how much heat a greenhouse gas traps in the atmosphere over a specific time relative to the same mass of CO_2. For CH_4, we use a 100-year global warming potential (GWP-100) of 27 and a 20-year global warming potential (GWP-20) of 80 (Forster et al., 2021). For N_2O, the GWP-100 and GWP-20 are both 273 due to its longer atmospheric lifetime (Forster et al., 2021). Although contemporaneous measurements of CO_2 are not available, we use surface pCO_2 measurements by Wallace and Gobler (2021) collected in 2014 in western LIS (the most recent and comprehensive data available) to provide an initial and approximate evaluation of the relative importance of CO_2, CH_4 and N_2O emissions from western LIS. At station MID4, which was named B3 in the study of Wallace and Gobler (2021), surface pCO_2 was ~600 μatm in June, July, and August 2014 and increased to 1300 μatm in September 2014 when the water column became well mixed and CO_2-rich subsurface waters were ventilated. At station EXCR (named A4 in their study), Wallace and Gobler (2021) measured surface pCO_2 averaging 800 μatm in June, 1300 μatm in July, 1200 μatm in August, and 1300 μatm in September. At both stations, the water column was mixed in September (vertical salinity gradient 0.2 PSS or less) and stratified in the other months. Using the wind speeds measured in 2023–2024 and the pCO_2 concentrations from June–September 2014, the estimated CO_2 fluxes averaged ~0.8 g CO_2 m^{-2} d^{-1} at MID4 and ~2 g CO_2 m^{-2} d^{-1} at EXCR. Using our CH_4 data from August, October and May, we calculated an average CH_4 flux at MID4 of ~0.03 g CO_2e m^{-2} d^{-1} (GWP-100) and ~0.08 g CO_2e m^{-2} d^{-1} (GWP-20). We similarly calculated an average CH_4 flux at EXCR of ~0.08 g CO_2e m^{-2} d^{-1} (GWP-100) and 0.2 g CO_2e m^{-2} d^{-1} (GWP-20). By the same method, we calculated an N_2O flux at MID4 averaging ~0.03 g CO_2e m^{-2} d^{-1} and at EXCR averaging ~0.05 g CO_2e m^{-2} d^{-1} (GWP-100 and GWP-20). We conclude that CO_2 is likely the dominant contributor to radiative forcing from western LIS. From our rough calculation, over a 100-year timescale, N_2O and CH_4 emissions each likely generate ≤5% of the radiative forcing caused by CO_2, and over a 20-year timescale, the radiative forcing of CH_4 is still likely ≤10% of the radiative forcing of CO_2. These results could be further refined through future studies in LIS measuring all three gases simultaneously.

3.8 Western LIS sea-air CH_4 and N_2O fluxes and concentrations in the global context

In general, the CH_4 and N_2O fluxes we estimate for western LIS fall within the range of prior studies which have concluded that estuaries play a small role in the global CH_4 and N_2O budgets. Globally, CH_4 and N_2O concentrations and sea-air fluxes from estuarine systems are highly variable and have a positively skewed distribution (Rosentreter et al., 2021; Zheng et al., 2022).

The sea-air CH_4 fluxes we estimate for western LIS (annual mean of 106 µmol m^{-2} d^{-1} and median of 66 µmol m^{-2} d^{-1}) and surface concentrations (annual mean of 78 nmol kg^{-1} and median of 50 nmol kg^{-1}) suggest that CH_4 dynamics in western LIS are consistent with other estuarine systems. A recent global metanalysis by Rosentreter et al. (2021) reported a mean estuarine CH_4 flux of 151 µmol m^{-2} d^{-1} and a median of 38 µmol m^{-2} d^{-1} (N = 53 sites), and a similar study by Zheng et al. (2022) reported a mean diffusive estuarine CH_4 flux of 780 µmol m^{-2} d^{-1} and a median of 120 µmol m^{-2} d^{-1} (N = 91 sites). The estuarine concentrations reported in Zheng et al. (2022) had a mean of 230 nmol kg^{-1} and a median of 110 nmol kg^{-1} – comparable to our results in western LIS. The maximum estuarine concentration reported in the metanalysis was 2300 nmol kg^{-1} and the maximum diffusive flux was 27,000 µmol m^{-2} d^{-1} (Zheng et al., 2022). Because of the positively skewed distribution, results for global upscaling of estuarine fluxes are highly sensitive to the dataset and model used (Rosentreter et al., 2021; Zheng et al., 2022). We note that the fluxes we report are for diffusive processes only. Ebullitive fluxes can be a significant contributor to CH_4 emissions in very shallow aquatic systems (bottom depths ~5 m or less), but in deeper systems such as western LIS (bottom depths ranging from 13 to 32 m at the stations in this study), diffusive fluxes will dominate as the vast majority of bubbles released from the sediment will dissolve before reaching the surface (Joyce and Jewell, 2003; West et al., 2016). Globally, estuaries are thought to contribute emissions of 1–6 Tg CH_4 y^{-1} based on mean fluxes from global data compilations (Rosentreter et al., 2021; Zheng et al., 2022), which is ≤1% of global CH_4 emissions from both natural and anthropogenic sources, currently estimated at 540–865 Tg CH_4 y^{-1} (Saunois et al., 2025).

Our N_2O fluxes, estimated to have an annual mean of 3.7 µmol m^{-2} d^{-1} and median of 3.2 µmol m^{-2} d^{-1} are comparable to, though on the low end, of published typical ranges for estuaries. For example, the global metanalysis of Zheng et al. (2022) reported a mean estuarine N_2O water-air flux of 19 µmol m^{-2} d^{-1} and a median of 6 µmol m^{-2} d^{-1} (minimum −7 µmol m^{-2} d^{-1}, maximum 177 µmol m^{-2} d^{-1}) based on 83 studies. Their study demonstrates that a few sites with elevated N_2O significantly influence their global average, causing the mean to be substantially larger than the median. Their mean estuarine N_2O concentration of 32 nmol kg^{-1} and median of 15 nmol kg^{-1} (minimum 4 nmol kg^{-1}, maximum 210 nmol kg^{-1}) are also comparable, though trending somewhat higher than the concentrations we observed (annual mean of 11.5 nmol kg^{-1} and median of 11.1

nmol kg^{-1} for surface waters). Globally, N_2O emissions from inland waters, estuaries and coastal vegetation were estimated for the year 2020 as 0.1 (range 0–0.2) Tg N y^{-1}, which is small in comparison to total net N_2O emissions from all anthropogenic and natural sources, estimated at 18.5 Tg N y^{-1} (range 10.6–27.0 Tg N y^{-1}) from bottom-up approaches that incorporate flux measurements, data-based nitrogen inventories, and models (Tian et al., 2024). The study of Zheng et al. (2022) estimated a higher flux of ~0.25 Tg N y^{-1} from estuaries alone, indicating that although uncertainty persists in global estuarine fluxes due to the uncertainties in upscaling fluxes with a positively skewed distribution, estuaries likely play a small role in to the global N_2O budget.

4. Conclusions

We have obtained the first measurements of the greenhouse gases CH_4 and N_2O in western LIS, a eutrophic urban estuary, in spring, summer, and fall. Although both gases can be generated under processes associated with organic matter remineralization and low-oxygen conditions in subsurface waters, we found that both CH_4 and N_2O often displayed higher concentrations at the surface compared to the subsurface. Both gases showed a lateral (along-estuary) gradient in the near-surface, and concentrations in the upper 10 m were highest at the westernmost station (closest to the East River and New York City) in all three seasons. Conversely, near-surface O_2 concentrations were typically lowest at the westernmost stations and decreased eastward. Hypoxia is most pronounced in late summer (August), and these low O_2 conditions were associated with elevated CH_4 concentrations and sea-air fluxes. However, N_2O concentrations and fluxes were highest in May, indicating that biogeochemical processes associated with seasonal hypoxia are not the primary driver of N_2O dynamics in western LIS. Repeat measurements at station MID4 suggested that sub-daily variability in O_2, CH_4, and N_2O concentrations were influenced by multiple factors and could not be correlated solely to daily changes in light or tidal phase. Sea-air fluxes of CH_4 and N_2O were comparable with other estuaries worldwide.

Our dataset suggests there is a persistent source of fresh surface water elevated in CH_4 and N_2O (or substrates that support production of these gases) to western LIS which enhances surface concentrations and sea-air fluxes in this region. Given the shallow mixed layer depths in western LIS for most of the year, these concentrations will be quickly released to the atmosphere. The residence time of both gases in the mixed layer with respect to gas exchange was 4 days on average in our study (calculated from the ratio of the mixed layer depth to the gas transfer velocity). We suggest that future work could focus on mapping the distributions of these gases in the East River and in proximity to wastewater inputs. To determine production and consumption mechanisms and rates, water column incubation experiments could be combined with metagenomic analyses (Bourbonnais et al., 2021; Euler et al., 2020; Karl et al., 2008; Rasmussen and Francis, 2022; Uhlig and Loose, 2017). Furthermore, coupled measurements of CO_2, CH_4, and N_2O could improve quantification of the relative importance of these three gases in contributing to total global warming potential from this region. Western LIS is experiencing ongoing biogeochemical changes including reductions in nutrient loading, warming and associated reductions in O_2 solubility, and acidification driven by increases in atmospheric CO_2 levels (Wallace and Gobler, 2021; Whitney and Vlahos, 2021). Continued monitoring along with targeted experiments evaluating the impacts of multiple stressors would improve predictions of how projected future changes will influence greenhouse gas emissions (Tang et al., 2024a).

Data accessibility statement: The following datasets were generated.

Manning, CCM; Payyambally, A; Mottram, J; Ward, K (2026): Methane and nitrous oxide dissolved gas concentrations from western Long Island Sound [dataset].
PANGAEA, https://doi.org/10.1594/PANGAEA.987944

Manning, CCM; Payyambally, A; Mottram, J; Ward, K (2026): Methane and nitrous oxide sea-air fluxes from western Long Island Sound [dataset]. PANGAEA, https://doi.org/10.1594/PANGAEA.987952

Contributions:
Contributed to conception and design: CM, AP, KW
Contributed to acquisition of data: CM, AP, JM, KW
Contributed to analysis and interpretation of data: CM
Drafted and/or revised the article: CM, AP, JM, KW
Approved the submitted version for publication: CM, AP, JM, KW

Acknowledgements:
We thank the captain, crew, and science teams on the trips for their support of the research. We thank Julie Granger for providing feedback on a draft of the manuscript.

Funding: Ship time on the *R/V Connecticut* was funded through project R/CMC-20/CTNY funded under award LI-96196201, US Environmental Protection Agency, to the Sponsored Program Services of the University of Connecticut on behalf of Connecticut Sea Grant, and in collaboration with NYSG. The statements, findings, conclusions, views, and recommendations are those of the authors and do not necessarily reflect the views of any of those organizations. Acquisition of data at NOAA mooring 44022 used in this study was supported through the Long Island Sound Integrated Coastal Observatory (LISICOS) which is funded by NOAA. Additional funding for the research was provided by the University of Connecticut to CM.

Competing interests:
The authors declare no competing interests.

References

Alshboul, Z., Encinas-Fernández, J., Hofmann, H., and Lorke, A.: Export of Dissolved Methane and Carbon Dioxide with Effluents from Municipal Wastewater Treatment Plants, Environ. Sci. Technol., 50, 5555–5563, https://doi.org/10.1021/acs.est.5b04923, 2016.

Amaral, V., Ortega, T., Romera-Castillo, C., and Forja, J.: Linkages between greenhouse gases (CO2, CH4, and N2O) and dissolved organic matter composition in a shallow estuary, Science of The Total Environment, 788, 147863, https://doi.org/10.1016/j.scitotenv.2021.147863, 2021.

Anderson, T. H. and Taylor, G. T.: Nutrient pulses, plankton blooms, and seasonal hypoxia in western Long Island Sound, Estuaries, 24, 228–243, https://doi.org/10.2307/1352947, 2001.

Bange, H. W., Freing, A., Kock, A., and Löscher, C. R.: Marine Pathways to Nitrous Oxide, in: Nitrous Oxide and Climate Change, Routledge, 36–62, 2010.

Barrett, L. J., Vlahos, P., McGuinness, M. A., Whitney, M. M., and Vaudrey, J. M. P.: Droughts and deluges: changes in river discharge and the carbonate chemistry of an urbanized temperate estuary, Front. Mar. Sci., 11, https://doi.org/10.3389/fmars.2024.1398087, 2024.

Bennett, D. C., O’Donnell, J., Bohlen, W. F., and Houk, A.: Tides and Overtides in Long Island Sound, j mar res, 68, 1–35, https://doi.org/10.1357/002224010793079031, 2010.

Bianchi, D., Weber, T. S., Kiko, R., and Deutsch, C.: Global niche of marine anaerobic metabolisms expanded by particle microenvironments, Nature Geosci, 11, 263–268, https://doi.org/10.1038/s41561-018-0081-0, 2018.

Bittig, H. C., Körtzinger, A., Neill, C., van Ooijen, E., Plant, J. N., Hahn, J., Johnson, K. S., Yang, B., and Emerson, S. R.: Oxygen Optode Sensors: Principle, Characterization, Calibration, and Application in the Ocean, Front. Mar. Sci., 4, https://doi.org/10.3389/fmars.2017.00429, 2018.

Blumberg, A. F. and Pritchard, D. W.: Estimates of the transport through the East River, New York, Journal of Geophysical Research: Oceans, 102, 5685–5703, https://doi.org/10.1029/96JC03416, 1997.

Bourbonnais, A., Frey, C., Sun, X., Bristow, L. A., Jayakumar, A., Ostrom, N. E., Casciotti, K. L., and Ward, B. B.: Protocols for Assessing Transformation Rates of Nitrous Oxide in the Water Column, Front. Mar. Sci., 8, https://doi.org/10.3389/fmars.2021.611937, 2021.

Bowman, M. J.: Nutrient distributions and transport in Long Island Sound, Estuarine and Coastal Marine Science, 5, 531–548, https://doi.org/10.1016/0302-3524(77)90100-1, 1977.

Buck, N. J., Gobler, C. J., and Sañudo-Wilhelmy, S. A.: Dissolved Trace Element Concentrations in the East River−Long Island Sound System: Relative Importance of Autochthonous versus Allochthonous Sources, Environ. Sci. Technol., 39, 3528–3537, https://doi.org/10.1021/es048860t, 2005.

Burgos, M., Sierra, A., Ortega, T., and Forja, J. M.: Anthropogenic effects on greenhouse gas (CH4 and N2O) emissions in the Guadalete River Estuary (SW Spain), Science of The Total Environment, 503–504, 179–189, https://doi.org/10.1016/j.scitotenv.2014.06.038, 2015.

Capelle, D. W. and Tortell, P. D.: Factors controlling methane and nitrous-oxide variability in the southern British Columbia coastal upwelling system, 179, 56–67, https://doi.org/10.1016/j.marchem.2016.01.011, 2016.

Chen, M., Canelli, E., and Fuhs, G. W.: Effects of Salinity on Nitrification in the East River, Journal (Water Pollution Control Federation), 47, 2474–2481, 1975.

Damm, E., Thoms, S., Beszczynska-Möller, A., Nöthig, E. M., and Kattner, G.: Methane excess production in oxygen-rich polar water and a model of cellular conditions for this paradox, Polar Science, 9, 327–334, https://doi.org/10.1016/j.polar.2015.05.001, 2015.

Diaz, R. J. and Rosenberg, R.: Spreading Dead Zones and Consequences for Marine Ecosystems, Science, 321, 926–929, https://doi.org/10.1126/science.1156401, 2008.

Dlugokencky, E. J., Steele, L. P., Lang, P. M., and Masarie, K. A.: The growth rate and distribution of atmospheric methane, Journal of Geophysical Research: Atmospheres, 99, 17021–17043, https://doi.org/10.1029/94JD01245, 1994.

Dlugokencky, E. J., Crotwell, A. M., Mund, J. W., Crotwell, M. J., and Thoning, K. W.: Atmospheric Methane Dry Air Mole Fractions from the NOAA GML Carbon Cycle Cooperative Global Air Sampling Network, 1983-2019, Version: 2020-07, 2020a.

Dlugokencky, E. J., Crotwell, A. M., Mund, J. W., Crotwell, M. J., and Thoning, K. W.: Atmospheric Nitrous Oxide Dry Air Mole Fractions from the NOAA GML Carbon Cycle Cooperative Global Air Sampling Network, 1997-2019, Version: 2020-07, 2020b.

Duvall, M. S., Hagy, J. D., Ammerman, J. W., and Tedesco, M. A.: High-frequency Dissolved Oxygen Dynamics in an Urban Estuary, the Long Island Sound, Estuaries and Coasts, 47, 415–430, https://doi.org/10.1007/s12237-023-01278-8, 2024.

EPA: Inventory of U.S. Greenhouse Gas Emissions and Sinks: 1990-2020. U.S. Environmental Protection Agency, EPA 430-R-22-003, 2022.

Euler, S., Jeffrey, L. C., Maher, D. T., Mackenzie, D., and Tait, D. R.: Shifts in methanogenic archaea communities and methane dynamics along a subtropical estuarine land use gradient, PLOS ONE, 15, e0242339, https://doi.org/10.1371/journal.pone.0242339, 2020.

Fazi, S., Amalfitano, S., Venturi, S., Pacini, N., Vazquez, E., Olaka, L. A., Tassi, F., Crognale, S., Herzsprung, P., Lechtenfeld, O. J., Cabassi, J., Capecchiacci, F., Rossetti, S., Yakimov, M. M., Vaselli, O., Harper, D. M., and Butturini, A.: High concentrations of dissolved biogenic methane associated with cyanobacterial blooms in East African lake surface water, Commun Biol, 4, 845, https://doi.org/10.1038/s42003-021-02365-x, 2021.

Forster, P., Storelvmo, T., and Armour, K.: Chapter 7: The Earth's Energy Budget, Climate Feedbacks, and Climate Sensitivity, in: Climate Change 2021 – The Physical Science Basis: Working Group I Contribution to the Sixth Assessment Report of the Intergovernmental Panel on Climate Change, Cambridge University Press, 923–1054, 2021.

Gay, P. S., O’Donnell, J., and Edwards, C. A.: Exchange between Long Island Sound and adjacent waters, Journal of Geophysical Research: Oceans, 109, https://doi.org/10.1029/2004JC002319, 2004.

GEBCO Compilation Group: GEBCO 2024 Grid, https://dx.doi.org/10.5285/1c44ce99-0a0d-5f4f-e063-7086abc0ea0f, 2024.

Gobler, C. J., Buck, N. J., Sieracki, M. E., and Sañudo-Wilhelmy, S. A.: Nitrogen and silicon limitation of phytoplankton communities across an urban estuary: The East River-Long Island Sound system, Estuarine, Coastal and Shelf Science, 68, 127–138, https://doi.org/10.1016/j.ecss.2006.02.001, 2006.

Goebel, N. and Kremer, J.: Temporal and spatial variability of photosynthetic parameters and community respiration in Long Island Sound, Mar. Ecol. Prog. Ser., 329, 23–42, https://doi.org/10.3354/meps329023, 2007.

Gonsalves, M.-J., Fernandes, C. E. G., Fernandes, S. O., Kirchman, D. L., and Bharathi, P. A. L.: Effects of composition of labile organic matter on biogenic production of methane in the coastal sediments of the Arabian Sea, Environ Monit Assess, 182, 385–395, https://doi.org/10.1007/s10661-011-1883-3, 2011.

Hall, B. D., Dutton, G. S., and Elkins, J. W.: The NOAA nitrous oxide standard scale for atmospheric observations, Journal of Geophysical Research (Atmospheres), 112, 09305, 2007.

Hall, N., Wong, W. W., Lappan, R., Ricci, F., Jeppe, K. J., Glud, R. N., Kawaichi, S., Rotaru, A.-E., Greening, C., and Cook, P. L. M.: Coastal methane emissions driven by aerotolerant methanogens using seaweed and seagrass metabolites, Nat. Geosci., 1–8, https://doi.org/10.1038/s41561-025-01768-3, 2025.

Harley, J. F., Carvalho, L., Dudley, B., Heal, K. V., Rees, R. M., and Skiba, U.: Spatial and seasonal fluxes of the greenhouse gases N2O, CO2 and CH4 in a UK macrotidal estuary, Estuarine, Coastal and Shelf Science, 153, 62–73, https://doi.org/10.1016/j.ecss.2014.12.004, 2015.

Hayduk, W. and Laudie, H.: Prediction of diffusion coefficients for nonelectrolytes in dilute aqueous solutions, AIChE Journal, 20, 611–615, https://doi.org/10.1002/aic.690200329, 1974.

Howarth, R., Chan, F., Conley, D. J., Garnier, J., Doney, S. C., Marino, R., and Billen, G.: Coupled biogeochemical cycles: eutrophication and hypoxia in temperate estuaries and coastal marine ecosystems, Frontiers in Ecology and the Environment, 9, 18–26, https://doi.org/10.1890/100008, 2011.

Hsu, S. A., Meindl, E. A., and Gilhousen, D. B.: Determining the power-law wind-profile exponent under near-neutral stability conditions at sea, Journal of Applied …, 33, 757–765, https://doi.org/10.1175/1520-0450(1994)033%253C0757:DTPLWP%253E2.0.CO;2, 1994.

Irby, I. D., Friedrichs, M. A. M., Da, F., and Hinson, K. E.: The competing impacts of climate change and nutrient reductions on dissolved oxygen in Chesapeake Bay, Biogeosciences, 15, 2649–2668, https://doi.org/10.5194/bg-15-2649-2018, 2018.

Izett, R. W., Fennel, K., Stoer, A. C., and Nicholson, D. P.: Reviews and syntheses: expanding the global coverage of gross primary production and net community production measurements using Biogeochemical-Argo floats, Biogeosciences, 21, 13–47, https://doi.org/10.5194/bg-21-13-2024, 2024.

Jähne, B., Heinz, G., and Dietrich, W.: Measurement of the Diffusion Coefficients of Sparingly Soluble Gases in Water, J Geophys Res, 92, 10767–10776, https://doi.org/10.1029/JC092iC10p10767, 1987.

Jin, H., Yoon, T. K., Begum, M. S., Lee, E.-J., Oh, N.-H., Kang, N., and Park, J.-H.: Longitudinal discontinuities in riverine greenhouse gas dynamics generated by dams and urban wastewater, Biogeosciences, 15, 6349–6369, https://doi.org/10.5194/bg-15-6349-2018, 2018.

Joyce, J. and Jewell, P. W.: Physical controls on methane ebullition from reservoirs and lakes, Environmental & Engineering Geoscience, 9, 167–178, 2003.

Karl, D. M., Beversdorf, L., Björkman, K. M., Church, M. J., Martinez, A., and Delong, E. F.: Aerobic production of methane in the sea, Nature Geosci, 1, 473–478, https://doi.org/10.1038/ngeo234, 2008.

Klawonn, I., Bonaglia, S., Brüchert, V., and Ploug, H.: Aerobic and anaerobic nitrogen transformation processes in N2-fixing cyanobacterial aggregates, ISME J, 9, 1456–1466, https://doi.org/10.1038/ismej.2014.232, 2015.

Kock, A., Arévalo-Martínez, D. L., Löscher, C. R., and Bange, H. W.: Extreme N2O accumulation in the coastal oxygen minimum zone off Peru, Biogeosciences, 13, 827–840, https://doi.org/10.5194/bg-13-827-2016, 2016.

Lan, X., Nisbet, E. G., Dlugokencky, E. J., and Michel, S. E.: What do we know about the global methane budget? Results from four decades of atmospheric CH4 observations and the way forward, Philosophical Transactions of the Royal Society A: Mathematical, Physical and Engineering Sciences, 379, 20200440, https://doi.org/10.1098/rsta.2020.0440, 2021.

Langdon, C.: Determination of dissolved oxygen in seawater by Winkler titration using the amperometric technique, The GO-SHIP Repeat Hydrography Manual: A Collection of Expert Repots and Guidelines, IOCCP Report No. 14, ICPO Publication Series No. 134, 18, https://doi.org/10.25607/OBP-1350, 2010.

Lee, Y. J. and Lwiza, K.: Interannual variability of temperature and salinity in shallow water: Long Island Sound, New York, Journal of Geophysical Research: Oceans, 110, https://doi.org/10.1029/2004JC002507, 2005.

Lee, Y. J. and Lwiza, K. M. M.: Characteristics of bottom dissolved oxygen in Long Island Sound, New York, Estuarine, Coastal and Shelf Science, 76, 187–200, https://doi.org/10.1016/j.ecss.2007.07.001, 2008.

Leon-Palmero, E., Morales-Baquero, R., Thamdrup, B., Löscher, C., and Reche, I.: Sunlight drives the abiotic formation of nitrous oxide in fresh and marine waters, Science, 387, 1198–1203, https://doi.org/10.1126/science.adq0302, 2025.

Li, Y., Meseck, S. L., Dixon, M. S., and Wikfors, G. H.: The East River tidal strait, New York City, New York, a high-nutrient, low-chlorophyll coastal system, Int Aquat Res, 10, 65–77, https://doi.org/10.1007/s40071-018-0189-2, 2018.

Li, Y., Fichot, C. G., Geng, L., Scarratt, M. G., and Xie, H.: The Contribution of Methane Photoproduction to the Oceanic Methane Paradox, Geophysical Research Letters, 47, e2020GL088362, https://doi.org/10.1029/2020GL088362, 2020.

Maeck, A., Hofmann, H., and Lorke, A.: Pumping methane out of aquatic sediments – ebullition forcing mechanisms in an impounded river, Biogeosciences, 11, 2925–2938, https://doi.org/10.5194/bg-11-2925-2014, 2014.

Magen, C., Lapham, L. L., Pohlman, J. W., Marshall, K., Bosman, S., Casso, M., and Chanton, J. P.: A simple headspace equilibration method for measuring dissolved methane, Limnology and Oceanography: Methods, 12, 637–650, https://doi.org/10.4319/lom.2014.12.637, 2014.

Manning, C. C. M., Payyambally, A., Mottram, J., and Ward, K.: Methane and nitrous oxide dissolved gas concentrations from western Long Island Sound [dataset], https://doi.org/10.1594/PANGAEA.987944, 2026.

Martens, C. S. and Berner, R. A.: Methane Production in the Interstitial Waters of Sulfate-Depleted Marine Sediments, Science, 185, 1167–1169, https://doi.org/10.1126/science.185.4157.1167, 1974.

Martens, C. S. and Berner, R. A.: Interstitial water chemistry of anoxic Long Island Sound sediments. 1. Dissolved gases1, Limnology and Oceanography, 22, 10–25, https://doi.org/10.4319/lo.1977.22.1.0010, 1977.

Martini, M., Butman, B., and Mickelson, M. J.: Long-Term Performance of Aanderaa Optodes and Sea-Bird SBE-43 Dissolved-Oxygen Sensors Bottom Mounted at 32 m in Massachusetts Bay, https://doi.org/10.1175/JTECH2078.1, 2007.

Mau, S., Blees, J., Helmke, E., Niemann, H., and Damm, E.: Vertical distribution of methane oxidation and methanotrophic response to elevated methane concentrations in stratified waters of the Arctic fjord Storfjorden (Svalbard, Norway), Biogeosciences, 10, 6267–6278, https://doi.org/10.5194/bg-10-6267-2013, 2013.

Maya-Altamira, L., Baun, A., Angelidaki, I., and Schmidt, J. E.: Influence of wastewater characteristics on methane potential in food-processing industry wastewaters, Water Research, 42, 2195–2203, https://doi.org/10.1016/j.watres.2007.11.033, 2008.

Mazur, C. I., Al-Haj, A. N., Ray, N. E., Sanchez-Viruet, I., and Fulweiler, R. W.: Low denitrification rates and variable benthic nutrient fluxes characterize Long Island Sound sediments, Biogeochemistry, 154, 37–62, https://doi.org/10.1007/s10533-021-00795-7, 2021.

McCardell, G., O’Donnell, J., Souza, A. J., and Palmer, M. R.: Internal tides and tidal cycles of vertical mixing in western Long Island Sound, Journal of Geophysical Research: Oceans, 121, 1063–1084, https://doi.org/10.1002/2015JC010796, 2016.

Naqvi, S. W. A., Bange, H. W., Farías, L., Monteiro, P. M. S., Scranton, M. I., and Zhang, J.: Marine hypoxia/anoxia as a source of CH_4 and N_2O, Biogeosciences, 7, 2159–2190, https://doi.org/10.5194/bg-7-2159-2010, 2010.

Nevison, C., Butler, J. H., and Elkins, J. W.: Global distribution of N_2O and the ΔN_2O-AOU yield in the subsurface ocean, Global Biogeochemical Cycles, 17, https://doi.org/10.1029/2003GB002068, 2003.

Nicholson, D. P., Wilson, S. T., Doney, S. C., and Karl, D. M.: Quantifying subtropical North Pacific gyre mixed layer primary productivity from Seaglider observations of diel oxygen cycles, Geophysical Research Letters, 42, 4032–4039, https://doi.org/10.1002/2015GL063065, 2015.

NOAA: https://tidesandcurrents.noaa.gov/noaacurrents/predictions.html?id=LIS1035_12, last access: 4 October 2025.

NYCDEP: https://www.nyc.gov/site/dep/water/wastewater-treatment-plants.page, last access: 4 October 2025.

Nylund, A. T., Mellqvist, J., Conde, V., Salo, K., Bensow, R., Arneborg, L., Jalkanen, J.-P., Tengberg, A., and Hassellöv, I.-M.: Coastal methane emissions triggered by ship passages, Commun Earth Environ, 6, 380, https://doi.org/10.1038/s43247-025-02344-8, 2025.

O’Connor, D. J.: An Analysis of the Dissolved Oxygen Distribution in the East River, Journal (Water Pollution Control Federation), 38, 1813–1830, 1966.

O’Donnell, J., Dam, H. G., Bohlen, W. F., Fitzgerald, W., Gay, P. S., Houk, A. E., Cohen, D. C., and Howard-Strobel, M. M.: Intermittent ventilation in the hypoxic zone of western Long Island Sound during the summer of 2004, Journal of Geophysical Research: Oceans, 113, https://doi.org/10.1029/2007JC004716, 2008.

O’Donnell, J., Wilson, R. E., Lwiza, K., Whitney, M., Bohlen, W. F., Codiga, D., Fribance, D. B., Fake, T., Bowman, M., and Varekamp, J.: The Physical Oceanography of Long Island Sound, in: Long Island Sound, edited by: Latimer, J. S., Tedesco, M. A., Swanson, R. L., Yarish, C., Stacey, P. E., and Garza, C., Springer New York, New York, NY, 79–158, https://doi.org/10.1007/978-1-4614-6126-5_3, 2014.

Parker, C. A. and O’Reilly, J. E.: Oxygen Depletion in Long Island Sound: A Historical Perspective, Estuaries, 14, 248–264, 1991.

de la Paz, M., Ferrón, S., Borges, A. V., and Upstill-Goddard, R. C.: Quantification of dissolved methane and nitrous oxide via headspace equilibrium, https://orbi.uliege.be/bitstream/2268/253977/1/SOP5-OCB-Report-v6c.pdf, 2021.

Perez-Coronel, E. and Beman, J. M.: Multiple sources of aerobic methane production in aquatic ecosystems include bacterial photosynthesis, Nat Commun, 13, 6454, https://doi.org/10.1038/s41467-022-34105-y, 2022.

Peterse, I. F., Hendriks, L., Weideveld, S. T. J., Smolders, A. J. P., Lamers, L. P. M., Lücker, S., and Veraart, A. J.: Wastewater-effluent discharge and incomplete denitrification drive riverine CO2, CH4 and N2O emissions, Science of The Total Environment, 951, 175797, https://doi.org/10.1016/j.scitotenv.2024.175797, 2024.

Proctor, C., Coupel, P., Casciotti, K., Tremblay, J.-E., Zakem, E., Arrigo, K. R., and Mills, M. M.: Light, ammonium, pH, and phytoplankton competition as environmental factors controlling nitrification, Limnology and Oceanography, 68, 1490–1503, https://doi.org/10.1002/lno.12359, 2023.

Rasmussen, A. N. and Francis, C. A.: Genome-Resolved Metagenomic Insights into Massive Seasonal Ammonia-Oxidizing Archaea Blooms in San Francisco Bay, mSystems, 7, e01270-21, https://doi.org/10.1128/msystems.01270-21, 2022.

Reeburgh, W.: Oceanic methane biogeochemistry, American Chemical Society, 107, 486–513, https://doi.org/10.1021/cr050362v, 2007.

Repeta, D. J., Ferrón, S., Sosa, O. A., Johnson, C. G., Repeta, L. D., Acker, M., Delong, E. F., and Karl, D. M.: Marine methane paradox explained by bacterial degradation of dissolved organic matter, Nature Geosci, 9, 884–887, https://doi.org/10.1038/ngeo2837, 2016.

Reuer, M., Barnett, B., Bender, M., Falkowski, P., and Hendricks, M.: New estimates of Southern Ocean biological production rates from O2/Ar ratios and the triple isotope composition of O2, Deep Sea Research Part I: Oceanographic Research, 54, 951–974, 2007.

Robinson, A. D., Nedwell, D. B., Harrison, R. M., and Ogilvie, B. G.: Hypernutrified estuaries as sources of N 2 O emission to the atmosphere: the estuary of the River Colne, Essex, UK, Marine Ecology Progress Series, 164, 59–71, 1998.

Römer, M., Riedel, M., Scherwath, M., Heesemann, M., and Spence, G. D.: Tidally controlled gas bubble emissions: A comprehensive study using long-term monitoring data from the NEPTUNE cabled observatory offshore Vancouver Island, Geochem. Geophys. Geosyst., 1–18, https://doi.org/10.1002/2016GC006528, 2016.

Rosentreter, J. A., Borges, A. V., Deemer, B. R., Holgerson, M. A., Liu, S., Song, C., Melack, J., Raymond, P. A., Duarte, C. M., Allen, G. H., Olefeldt, D., Poulter, B., Battin, T. I., and Eyre, B. D.: Half of global methane emissions come from highly variable aquatic ecosystem sources, Nat. Geosci., 14, 225–230, https://doi.org/10.1038/s41561-021-00715-2, 2021.

Saunois, M., Martinez, A., Poulter, B., Zhang, Z., Raymond, P. A., Regnier, P., Canadell, J. G., Jackson, R. B., Patra, P. K., Bousquet, P., Ciais, P., Dlugokencky, E. J., Lan, X., Allen, G. H., Bastviken, D., Beerling, D. J., Belikov, D. A., Blake, D. R., Castaldi, S., Crippa, M., Deemer, B. R., Dennison, F., Etiope, G., Gedney, N., Höglund-Isaksson, L., Holgerson, M. A., Hopcroft, P. O., Hugelius, G., Ito, A., Jain, A. K., Janardanan, R., Johnson, M. S., Kleinen, T., Krummel, P. B., Lauerwald, R., Li, T., Liu, X., McDonald, K. C., Melton, J. R., Mühle, J., Müller, J., Murguia-Flores, F., Niwa, Y., Noce, S., Pan, S., Parker, R. J., Peng, C., Ramonet, M., Riley, W. J., Rocher-Ros, G., Rosentreter, J. A., Sasakawa, M., Segers, A., Smith, S. J., Stanley, E. H., Thanwerdas, J., Tian, H., Tsuruta, A., Tubiello, F. N., Weber, T. S., van der Werf, G. R., Worthy, D. E. J., Xi, Y., Yoshida, Y., Zhang, W., Zheng, B., Zhu, Q., Zhu, Q., and Zhuang, Q.: Global Methane Budget 2000–2020, Earth System Science Data, 17, 1873–1958, https://doi.org/10.5194/essd-17-1873-2025, 2025.

Seitzinger, S. P., Kroeze, C., and Styles, R. V.: Global distribution of N2O emissions from aquatic systems: natural emissions and anthropogenic effects, Chemosphere: Global Change Science, 2, 267–279, https://doi.org/10.1016/S1465-9972(00)00015-5, 2000.

Smith, J. M., Chavez, F. P., and Francis, C. A.: Ammonium Uptake by Phytoplankton Regulates Nitrification in the Sunlit Ocean, PLoS ONE, 9, e108173, https://doi.org/10.1371/journal.pone.0108173, 2014.

Tang, K. W., McGinnis, D. F., Frindte, K., Brüchert, V., and Grossart, H.-P.: Paradox reconsidered: Methane oversaturation in well-oxygenated lake waters, Limnology and Oceanography, 59, 275–284, https://doi.org/10.4319/lo.2014.59.1.0275, 2014.

Tang, W., Da, F., Tracey, J. C., Intrator, N., Kunes, M. A., Lee, J. A., Wan, X. S., Jayakumar, A., Friedrichs, M. A. M., and Ward, B. B.: Nutrient management offsets the effect of deoxygenation and warming on nitrous oxide emissions in a large US estuary, Sci. Adv., 10, eadq5014, https://doi.org/10.1126/sciadv.adq5014, 2024a.

Tang, W., Talbott, J., Jones, T., and Ward, B. B.: Variable contribution of wastewater treatment plant effluents to downstream nitrous oxide concentrations and emissions, Biogeosciences, 21, 3239–3250, https://doi.org/10.5194/bg-21-3239-2024, 2024b.

Teeter, L., Hamme, R. C., Ianson, D., and Bianucci, L.: Accurate Estimation of Net Community Production From O_2/Ar Measurements, Global Biogeochemical Cycles, 32, 1163–1181, https://doi.org/10.1029/2017GB005874, 2018.

Thierry, V., Bittig, H., Gilbert, D., Kobayashi, T., Kanako, S., and Schmid, C.: Processing Argo oxygen data at the DAC level, Ifremer, https://doi.org/10.13155/39795, 2025.

Tian, H., Pan, N., Thompson, R. L., Canadell, J. G., Suntharalingam, P., Regnier, P., Davidson, E. A., Prather, M., Ciais, P., Muntean, M., Pan, S., Winiwarter, W., Zaehle, S., Zhou, F., Jackson, R. B., Bange, H. W., Berthet, S., Bian, Z., Bianchi, D., Bouwman, A. F., Buitenhuis, E. T., Dutton, G., Hu, M., Ito, A., Jain, A. K., Jeltsch-Thömmes, A., Joos, F., Kou-Giesbrecht, S., Krummel, P. B., Lan, X., Landolfi, A., Lauerwald, R., Li, Y., Lu, C., Maavara, T., Manizza, M., Millet, D. B., Mühle, J., Patra, P. K., Peters, G. P., Qin, X., Raymond, P., Resplandy, L., Rosentreter, J. A., Shi, H., Sun, Q., Tonina, D., Tubiello, F. N., van der Werf, G. R., Vuichard, N., Wang, J., Wells, K. C., Western, L. M., Wilson, C., Yang, J., Yao, Y., You, Y., and Zhu, Q.: Global nitrous oxide budget (1980–2020), Earth System Science Data, 16, 2543–2604, https://doi.org/10.5194/essd-16-2543-2024, 2024.

Uhlig, C. and Loose, B.: Using stable isotopes and gas concentrations for independent constraints on microbial methane oxidation at Arctic Ocean temperatures, Limnol. Oceanogr. Methods, 15, 737–751, https://doi.org/10.1002/lom3.10199, 2017.

NDBC: https://www.ndbc.noaa.gov/station_page.php?station=44022, last access: 4 October 2025.

Valentine, D. L.: Emerging Topics in Marine Methane Biogeochemistry, Annual Review of Marine Science, 3, 147–171, https://doi.org/10.1146/annurev-marine-120709-142734, 2011.

Vaquer-Sunyer, R. and Duarte, C. M.: Thresholds of hypoxia for marine biodiversity, Proceedings of the National Academy of Science, 105, 15452–15457, 2008.

Varekamp, J. C., McElroy, A. E., Mullaney, J. R., and Breslin, V. T.: Metals, Organic Compounds, and Nutrients in Long Island Sound: Sources, Magnitudes, Trends, and Impacts, in: Long Island Sound, edited by: Latimer, J. S., Tedesco, M. A., Swanson, R. L., Yarish, C., Stacey, P. E., and Garza, C., Springer New York, New York, NY, 203–283, https://doi.org/10.1007/978-1-4614-6126-5_5, 2014.

Vaudrey, J.: NEW YORK CITY'S IMPACT ON LONG ISLAND SOUND WATER QUALITY TECHNICAL REPORT, 2017.

Vlahos, P. and Whitney, M. M.: Organic carbon patterns and budgets in the Long Island Sound estuary, Limnology and Oceanography, 62, S46–S57, https://doi.org/10.1002/lno.10638, 2017.

Vlahos, P., Whitney, M. M., Menniti, C., Mullaney, J. R., Morrison, J., and Jia, Y.: Nitrogen budgets of the Long Island Sound estuary, Estuarine, Coastal and Shelf Science, 232, 106493, https://doi.org/10.1016/j.ecss.2019.106493, 2020.

Wallace, R. B.: Coastal Ocean Acidification: Dynamics and Potential to Affect Marine Mollusks, State University of New York at Stony Brook, 2020.

Wallace, R. B. and Gobler, C. J.: The role of algal blooms and community respiration in controlling the temporal and spatial dynamics of hypoxia and acidification in eutrophic estuaries, Marine Pollution Bulletin, 172, 112908, https://doi.org/10.1016/j.marpolbul.2021.112908, 2021.

Wan, X. S., Sheng, H.-X., Dai, M., Casciotti, K. L., Church, M. J., Zou, W., Liu, L., Shen, H., Zhou, K., Ward, B. B., and Kao, S.-J.: Epipelagic nitrous oxide production offsets carbon sequestration by the biological pump, Nat. Geosci., 16, 29–36, https://doi.org/10.1038/s41561-022-01090-2, 2023a.

Wan, X. S., Sheng, H.-X., Liu, L., Shen, H., Tang, W., Zou, W., Xu, M. N., Zheng, Z., Tan, E., Chen, M., Zhang, Y., Ward, B. B., and Kao, S.-J.: Particle-associated denitrification is the primary source of N2O in oxic coastal waters, Nat Commun, 14, 8280, https://doi.org/10.1038/s41467-023-43997-3, 2023b.

Wanninkhof, R.: Relationship between wind speed and gas exchange over the ocean revisited, Limnology and Oceanography: Methods, 12, 351–362, https://doi.org/10.4319/lom.2014.12.351, 2014.

Wanninkhof, R., Asher, W. E., Ho, D. T., Sweeney, C., and McGillis, W. R.: Advances in Quantifying Air-Sea Gas Exchange and Environmental Forcing, Annual Review of Marine Science, 1, 213–244, https://doi.org/10.1146/annurev.marine.010908.163742, 2009.

Ward, B. B.: Nitrification in Marine Systems, in: Nitrogen in the Marine Environment, edited by: Capone, D. G., Bronk, D. A., Molholland, M. R., and Carpenter, E. J., Elsevier, 199–261, 2008.

Ward, B. B., Kilpatrick, K. A., Novelli, P. C., and Scranton, M. I.: Methane Oxidation and Methane Fluxes in the Ocean Surface-Layer and Deep Anoxic Waters, Nature, 327, 226–229, 1987.

Weiss, R. F. and Price, B. A.: Nitrous oxide solubility in water and seawater, Marine Chemistry, 8, 347–359, https://doi.org/10.1016/0304-4203(80)90024-9, 1980.

West, W. E., Creamer, K. P., and Jones, S. E.: Productivity and depth regulate lake contributions to atmospheric methane, Limnology and Oceanography, 61, S51–S61, https://doi.org/10.1002/lno.10247, 2016.

Whitney, M. M. and Vlahos, P.: Reducing Hypoxia in an Urban Estuary Despite Climate Warming, Environ. Sci. Technol., 55, 941–951, https://doi.org/10.1021/acs.est.0c03964, 2021.

Wiesenburg, D. A. and Guinasso, N. L.: Equilibrium solubilities of methane, carbon monoxide, and hydrogen in water and sea water, Journal of Chemical & Engineering Data, 24, 356–360, https://doi.org/10.1021/je60083a006, 1979.

de Wilde, H. P. J. and de Bie, M. J. M.: Nitrous oxide in the Schelde estuary: production by nitrification and emission to the atmosphere, Marine Chemistry, 69, 203–216, https://doi.org/10.1016/S0304-4203(99)00106-1, 2000.

Wilke, C. R. and Chang, P.: Correlation of diffusion coefficients in dilute solutions, AIChE Journal, 1, 264–270, https://doi.org/10.1002/aic.690010222, 1955.

Wilson, R. E., Swanson, R. L., and Crowley, H. A.: Perspectives on long-term variations in hypoxic conditions in western Long Island Sound, Journal of Geophysical Research: Oceans, 113, https://doi.org/10.1029/2007JC004693, 2008.

Wilson, S. T., Bange, H. W., Arévalo-Martínez, D. L., Barnes, J., Borges, A. V., Brown, I., Bullister, J. L., Burgos, M., Capelle, D. W., Casso, M., de la Paz, M., Farías, L., Fenwick, L., Ferrón, S., Garcia, G., Glockzin, M., Karl, D. M., Kock, A., Laperriere, S., Law, C. S., Manning, C. C., Marriner, A., Myllykangas, J.-P., Pohlman, J. W., Rees, A. P., Santoro, A. E., Tortell, P. D., Upstill-Goddard, R. C., Wisegarver, D. P., Zhang, G.-L., and Rehder, G.: An intercomparison of oceanic methane and nitrous oxide measurements, Biogeosciences, 15, 5891–5907, https://doi.org/10.5194/bg-15-5891-2018, 2018.

Wrage, N., Velthof, G., and Van Beusichem, M.: Role of nitrifier denitrification in the production of nitrous oxide, Soil Biology and …, 2001.

Yin, H., Wang, Y., and Huang, J.: Photodegradation-induced biological degradation of treated wastewater effluent organic matter in receiving waters, Water Research, 204, 117567, https://doi.org/10.1016/j.watres.2021.117567, 2021.

Young, C., Martin, J. B., and Hanson, G. N.: Controls on Nitrous Oxide Production in, and Fluxes from a Coastal Aquifer in Long Island, NY, USA, Journal of Marine Science and Engineering, 4, 71, https://doi.org/10.3390/jmse4040071, 2016.

Yu, C., He, Q., Nie, W.-B., Zhang, T., Wu, H., Yang, Y., Fu, S., Tan, X., and Chen, Y.: Effluent organic matter facilitates anaerobic methane oxidation coupled with nitrous oxide reduction in river sediments, Water Research, 278, 123415, https://doi.org/10.1016/j.watres.2025.123415, 2025.

Zakem, E. J. and Follows, M. J.: A theoretical basis for a nanomolar critical oxygen concentration, Limnology and Oceanography, 62, 795–805, https://doi.org/10.1002/lno.10461, 2017.

Zakem, E. J., Mahadevan, A., Lauderdale, J. M., and Follows, M. J.: Stable aerobic and anaerobic coexistence in anoxic marine zones, ISME J, 14, 288–301, https://doi.org/10.1038/s41396-019-0523-8, 2020.

Zheng, X., Mei, B., Wang, Y., Xie, B., Wang, Y., Dong, H., Xu, H., Chen, G., Cai, Z., Yue, J., Gu, J., Su, F., Zou, J., and Zhu, J.: Quantification of N2O fluxes from soil–plant systems may be biased by the applied gas chromatograph methodology, Plant Soil, 311, 211–234, https://doi.org/10.1007/s11104-008-9673-6, 2008.

Zheng, Y., Wu, S., Xiao, S., Yu, K., Fang, X., Xia, L., Wang, J., Liu, S., Freeman, C., and Zou, J.: Global methane and nitrous oxide emissions from inland waters and estuaries, Global Change Biology, 28, 4713–4725, https://doi.org/10.1111/gcb.16233, 2022.